Electroanalytical Chemistry and Interfacial Electrochemistry, 53 (1974) 1–55

BINARY ELECTROLYTE SMALL-SIGNAL FREQUENCY RESPONSE

J. ROSS MACDONALD

Texas Instruments Incorporated, MS-227, P.O. Box 5474, Dallas, Texas 75222 (U.S.A.)
(Received 30th November 1973)

I. INTRODUCTION

Interest is rapidly growing in the frequency response of a variety of binary charge systems. In such systems, two types of charge carrier are dominant; they have opposite signs and may have any mobility values, including zero for one of them. Representative systems include aqueous or other liquid electrolytes without a supporting electrolyte, glass electrodes, fused salts, and a variety of solid materials. Electrodes may be completely blocking for the charge carriers or may allow a conduction current, often involving an electrode reaction, to occur. Systems of the type considered are not purely ohmic at all frequencies, even neglecting their omnipresent geometric capacitance, C_g, but usually exhibit strong frequency-dependent capacitative and resistive effects.

In earlier work[1–4], some discussion of experimental results and of the various theories put forward to explain these small-signal frequency response results has been presented. In particular, considerable analysis has been given of the uni–univalent situation with equal mobilities for the two types of carriers[1–3]. Recently, a detailed theory has been published which involves arbitrary valences and mobilities and relatively general electrode boundary conditions[4]. It does not include specific ionic adsorption explicitly, however. This microscopic, charge-motion theory neglects no diffusion terms and yields results which satisfy Poisson's equation exactly everywhere within the material considered. Although the new theory applies in the fully dissociated extrinsic conduction situation as well as for intrinsic conditions, only the latter type of conduction will be considered in the present paper. Thus, the response of heavily doped solids at low temperatures is not covered by the present work and will be considered elsewhere[5].

The general theory[4] yields an exact analytic result for system impedance as a function of frequency, but this result depends on many parameters and is far too complex to be immediately transparent. In the earlier work[4], therefore, only its limit as the applied frequency goes to zero has been considered in detail. The purpose of the present paper is to (a) use computer calculations of the exact expression for total impedance to show some of the major types of frequency response to which the theory leads in the intrinsic case; (b) derive from the results simple approximate frequency response formulas for cases of especial interest; (c) present several approximate equivalent circuits applicable over limited frequency ranges and made up only of essentially frequency-independent elements together with Warburg circuit elements (where appropriate); and (d) finally to compare unsupported and supported results where pertinent. Frequency response will be shown by means of impedance-plane plots, by curves showing frequency dependence of the real and imaginary parts of the total impedance of the system, and by frequency response plots of its total parallel capacitance and conductance, derived from the total admittance. All of these types of presentations (and many more) have been used in showing small-signal response in the electrolyte, dielectric, and semiconductor fields. Although they involve some or all of the same information in different ways, all these methods are separately useful in comparing experimental and theoretical results. The presentation of all these approaches should also help make those authors who only use one method exclusively more aware of the virtues of other methods.

Note that although the analytic results of the general theory[4] depend on a linearizing assumption and thus apply in principle only for small-signal conditions, they need not necessarily be limited only to electrolyte situations where the potential of zero electrode charge and the equilibrium potential coincide. In the absence of specific adsorption but even in the presence of a non-zero direct current, the theoretical results[4] may apply provided the system is sufficiently linear around the bias point that the static components of charge are essentially constant and independent of position within the material considered. There is then no static field gradient in the material. Also, under these conditions an applied a.c. potential amplitude appreciably greater than kT/e may be applied as well without necessarily destroying the applicability of the theory[6]. Here k is Boltzmann's constant, T the absolute temperature, and e the protonic charge.

Although full comparison of theory and experiment requires (or derives) knowledge of the individual valence numbers z_p and z_n and of the individual mobilities μ_p and μ_n of the positive charge carriers (bulk concentration p_i) and negative charge carriers (bulk concentration n_i), in the normalized form of the theory only the ratios $\pi_z \equiv z_n/z_p$ and $\pi_m \equiv \mu_n/\mu_p$ are necessary[4]. For convenience and greatest generality many of the frequency response curves presented herein will thus involve normalized quantities. As we shall see, however, elimination of normalization when necessary is a simple process.

Finally, the description of a given space-charge situation with electrodes completely blocking or able to sustain charge transfer reactions requires parameters which define the specific boundary conditions at the electrodes. In the general theory, these dimensionless parameters are denoted r_p and r_n. When two identical electrodes are considered, these parameters are taken to be the same at both. Complete blocking occurs when $r_p = r_n = 0$. On the other hand, for example, when $r_p = 0$ and $r_n = \infty$, a condition we shall frequently consider herein, positive carriers are completely blocked and negative ones completely free to discharge or to appear at the electrodes. The condition $r_n = \infty$ is thus indicative of an infinitely rapid reaction rate for the negative carriers. The later presentation of theoretical results is facilitated through use of the derived boundary condition quantities $g_p \equiv 1 + (r_p/2)$ and $g_n \equiv 1 + (r_n/2)$. A glossary of symbols used herein is presented at the end of the paper.

II. BASIC EQUIVALENT CIRCUITS

The exact equivalent circuit found in the earlier work[4] is shown in Fig. 1a.

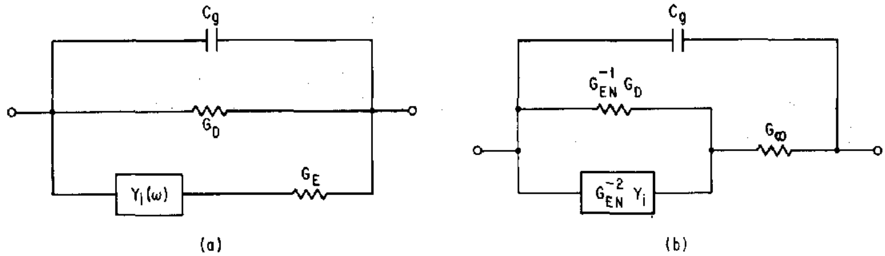

Fig. 1. Exact equivalent circuits involving the frequency-dependent admittance Y_i. The two circuits are electrically equivalent. Here $G_{EN} \equiv G_E/G_\infty$ and $G_\infty \equiv G_D + G_E$.

Figure 1b provides an alternative circuit which exhibits the same overall impedance, Z_T, as that of Fig. 1a at all frequencies. These circuits apply for the case of two identical plane-parallel electrodes separated by a distance l. The effects of any electrode roughness are ignored here. Most of the results considered herein apply to the situation of two identical electrodes, the usual one for solids. Modifications in element values to make circuits applicable for the usual aqueous electrolyte situation of a single small working electrode and a much larger indifferent electrode will be discussed later. A comparison will be made later of the present results with the conventional equivalent circuit used in the supported case (see Fig. 20a).

All circuit elements herein apply for unit electrode area. Thus, the geometrical capacitance C_g is given in the present case by $\varepsilon/4\pi l$, where ε is the dielectric constant of the basic material in the absence of mobile charge. Now let $Y_T \equiv Z_T^{-1} \equiv G_P + i\omega C_P$, where G_P and C_P are the parallel conductive and capacitative elements of the total admittance Y_T and ω is the radial frequency. It will be convenient hereafter to deal primarily with normalized quantities. Let us thus write $Y_{TN} \equiv G_{PN} + i\Omega C_{PN}$, where $\Omega \equiv \omega\tau_D \equiv \omega C_g R_\infty$. The subscript "N" will be used herein to indicate normalization of capacitances with C_g, resistances with R_∞, conductances with $G_\infty \equiv R_\infty^{-1}$, and time constants with τ_D. G_∞ is the high-frequency limiting conductance of the system and is given by $(e/l)(z_p\mu_p p_i + z_n\mu_n n_i)$, equal to $(e/2l)(z_p p_i + z_n n_i)(\mu_n + \mu_p)$ since $z_n n_i \equiv z_p p_i$ because of electroneutrality in the bulk[4].

The remaining elements appearing in the circuits of Fig. 1 are Y_i, G_E, and G_D. Only Y_i depends on frequency. The frequency dependences of the elements of $Z_i \equiv Y_i^{-1}$, R_i and C_i, will be considered in detail later. Note that we can write $Z_{iN} \equiv R_{iN} + (i\Omega C_{iN})^{-1}$. Finally, it turns out that $G_{EN} \equiv R_{EN}^{-1} \equiv g_s/g_p g_n$ and $G_{DN} \equiv R_{DN}^{-1} \equiv 1 - G_{EN}$. Thus, $G_E + G_D \equiv G_\infty$. Now $g_s \equiv g_p\varepsilon_n + g_n\varepsilon_p$, and g_p and g_n have already been defined. Here $\varepsilon_n \equiv (1+\pi_m^{-1})^{-1} = \mu_n/(\mu_n+\mu_p)$ and $\varepsilon_p \equiv (1+\pi_m)^{-1} = \mu_p/(\mu_n+\mu_p)$. These definitions lead to $G_{EN} \equiv \varepsilon_n[1+(r_n/2)]^{-1} + \varepsilon_p[1+(r_p/2)]^{-1}$ and $G_{DN} \equiv \varepsilon_n[1+(2/r_n)]^{-1} + \varepsilon_p[1+(2/r_p)]^{-1}$. Thus when $r_p = r_n = 0$, $G_{EN} = 1$ and $G_{DN} = 0$. On the other hand, when $r_p = 0$ and $r_n = \infty$, $G_{EN} = \varepsilon_p$ and $G_{DN} = \varepsilon_n$. Note that since in general $G_{EN}^{-1} G_{DN} = R_{EN} - 1$, the term $G_{EN}^{-1} G_D$ in Fig. 1b may be rewritten as $(R_{EN} - 1)G_\infty \equiv (R_{DN} - 1)^{-1} G_\infty$.

Figure 2a shows the low-frequency-limiting form of the circuit of Fig. 1a. Here the subscript "0" denotes the $\omega \to 0$ values. The exact formula for R_{iN0} is very lengthy, but various expressions for R_{iN0} in specific cases of interest have been given earlier[4]. The general expression for C_{iN0} is, however,

$$C_{iN0} = (g_p g_n)^{-2}[(\delta_n \delta_p M^2/3)(g_p - g_n)^2 + (r-1) g_z^2] \tag{1}$$

Here $\delta_n \equiv (1+\pi_z^{-1})^{-1} = z_n/(z_n+z_p)$, $\delta_p \equiv (1+\pi_z)^{-1} = z_p/(z_n+z_p)$, and $g_z \equiv g_p\delta_n + g_n\delta_p$. The quantity $M \equiv l/2L_D$ measures the number of Debye lengths contained in the half-cell distance $(l/2)$. In the present case

$$\begin{aligned} L_D &\equiv [\varepsilon kT/4\pi e^2(z_n^2 n_i + z_p^2 p_i)]^{\frac{1}{2}} \\ &= [\varepsilon kT\delta_n/4\pi e^2(z_n^2 n_i)]^{\frac{1}{2}} \\ &= [\varepsilon kT\delta_p/4\pi \varepsilon^2(z_p^2 p_i)]^{\frac{1}{2}} \end{aligned} \tag{2}$$

When the bulk concentrations n_i and p_i are given on a molar basis, k should be replaced by the gas constant R and e by F, the Faraday. Incidentally, many of the intrinsic conduction results of the present paper, such as Eqn. (1), apply also in the extrinsic case when ε_n, ε_p, δ_n, and δ_p are redefined for the extrinsic situation[4].

The quantity $r \equiv M\coth(M)$ in eqn. (1) will be essentially equal to M for all M values of usual interest. Since M may be far greater than unity, C_{iN0} also may be much greater than unity. Now when $r_p = r_n = 0$, the completely blocking electrodes condition, $C_{iN0} = r - 1$. The total low-frequency-limiting capacitance is then $C_{P0} \equiv C_g + C_{i0} = rC_g \cong MC_g = \varepsilon/8\pi L_D$. This is indeed, as it should be, the usual small-signal intensive double layer capacitance arising from two identical double layers in series[7]. Note that when $M \gg 1$ and $r_p \neq r_n$, eqn. (1) shows that C_{iN0} and C_{PN0} may greatly exceed the ordinary double-layer value. It is the large diffusion pseudo-capacitance represented by the first term of eqn. (1) that leads to the most interesting behavior inherent in the present situation. Such pseudocapacitance only appears when charges of opposite sign discharge unequally at the electrodes and is at a maximum when charge of one sign is completely blocked and the other completely free to discharge (*e.g.*, $r_p = 0$, $r_n = \infty$, or $r_p = \infty$, $r_n = 0$).

Figure 2b represents the high-frequency-limiting form of the equivalent

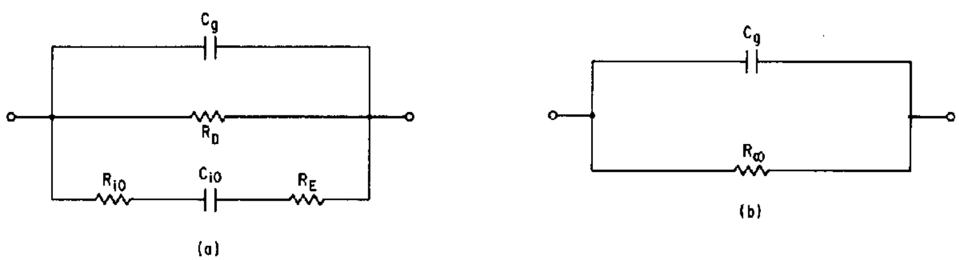

Fig. 2. (a) Low-frequency-limiting form of the circuit of Fig. 1; (b) high-frequency-limiting form.

circuits of Fig. 1. The remaining elements, C_g and R_∞, are of course independent of electrode boundary conditions in this frequency region defined by $\Omega \equiv \omega\tau_D > 0.1$. Note that for $\Omega = 1$, where ω is equal to the inverse of the basic dielectric relaxation time τ_D, the reactance associated with C_g is equal in magnitude to R_∞. If accurate measurements can be carried out for $\Omega > 0.1$, experimental values of C_g and R_∞ are best obtained from this region.

Finally, it will be useful to introduce the notation used in the earlier work[4] to designate a specific binary electrolyte situation: $(r_p, r_n; \pi_m, \pi_z; 0, M)$. Values of these normalized parameters, together with a value of Ω, entirely define a specific case of the theory in its normalized form; *i.e.*, they allow a specific value of Z_{TN} or Y_{TN} to be calculated. Because of the symmetry of the situation in normalized form, it turns out that for any Ω the case $(r_n, r_p; \pi_m^{-1}, \pi_z^{-1}; 0, M)$ yields the same value of Z_{TN} as does $(r_p, r_n; \pi_m, \pi_z; 0, M)$ for any specific set of values of these quantities. Thus, when a situation such as $(0, r_n; \pi_m, \pi_z; 0, M)$ is examined for a range of r_n values and for $\pi_m, \pi_z \gtrless 1$, it is unnecessary to consider separately the case $(r_p, 0; \pi_m, \pi_z; 0, M)$. For this reason, I shall here be concerned with, *e.g.*, $(0, \infty; \pi_m, \pi_z; 0, M)$, not with $(\infty, 0; \pi_m, \pi_z; 0, M)$.

III. IMPEDANCE-PLANE RESULTS

The circuits of Fig. 1 lead directly to the basic relation

$$Z_{TN} = \frac{(Z_{iN}+R_{EN})}{1+(i\Omega+G_{DN})(Z_{iN}+R_{EN})} \tag{3}$$

from which it is clear that when $|(i\Omega+G_{DN})(Z_{iN}+R_{EN})| \ll 1$, $(Z_{TN}-R_{EN}) \cong Z_{iN}$. One situation where the above condition holds is that for $(0, \infty; \pi_m, \pi_z; 0, M)$ with $10\,M^{-2} < (\Omega/\pi_m) < 1$ and $\pi_m \ll 1$, $M \gg 1$, and $\pi_m M < 1$. Then $G_{DN} = \varepsilon_n \cong \pi_m \ll 1$ and $R_{EN} = 1+\pi_m \cong 1 \equiv R_{\infty N}$. Thus, when the above conditions apply, simple subtraction of the bulk resistance R_∞ from the total measured impedance Z_T yields the "interface" impedance Z_i. As we shall see later, Z_i is not always a true interface impedance since it is not always completely intensive.

The above sort of results apply when charge of one sign is nearly or completely blocked, that of opposite sign discharges with an infinite or very large reaction rate, and the discharging charge carriers have a much smaller mobility than those that are completely or nearly completely blocked. As we shall see later, this is a very important and interesting case and is overtly consistent with the usual electrochemical practice of subtracting R_∞ from the total impedance in order to obtain intensive circuit element quantities associated with processes occurring near and at the working electrode.

Another case of some interest is that where

$$Z_{TN} \cong Z_{3N} \equiv (1+i\Omega)^{-1} \tag{4}$$

which yields simple Debye dispersion behavior with the single time constant τ_D. As we shall see, this is the usual result found with $M \gg 1$ under any other conditions at frequencies for which $\Omega > 0.1$. It follows immediately from eqn. (3) for the above $\pi_m \ll 1$ case when $|Z_{iN}| \ll R_{EN} \cong 1$. In addition, in the equal mobility case $(0, \infty; 1, \pi_z; 0, M)$, where $R_{EN}=2$ and $G_{DN}=0.5$, with $M \gg 1$ and when $|Z_{iN}| \ll R_{EN}$, eqn. (3) again leads to eqn. (4). Finally, the uninteresting case $(\infty, \infty; \pi_m, \pi_z; 0, M)$ involves just C_g and R_∞ in parallel and thus leads to $Z_{TN} = Z_{3N}$ at all frequencies.

One common way of delineating some aspects of impedance behavior is to show the circle diagram[8] or Cole–Cole plot[9], where the imaginary part of an impedance is plotted *versus* its real part with frequency as a parametric variable. Alternatively, admittance-plane circle diagrams may be plotted[2,10], as in early space-charge measurements on KBr[11]. Here, since their use seems somewhat more common, I shall present only impedance-plane[1 2] results and will later illustrate directly how the components of the total admittance depend on frequency. Figures 3–6 thus present impedance-plane plots, in terms of normalized quantities, for some specific (r_p, r_n; π_m, π_z; 0, M) cases of interest. Since the imaginary part of the normalized impedance is always capacitative, its negative has been used here for the ordinate scale. Note that infinite frequency occurs at the (0, 0) point and zero frequency is approached at the right. In addition, where appropriate, points corresponding to the three basic normalized frequency conditions $M^2\Omega=1$, $M\Omega=1$, and $\Omega=1$ have been shown on the curves of Figs. 3–6. The normalized parametric frequency variable Ω increases from right to left here.

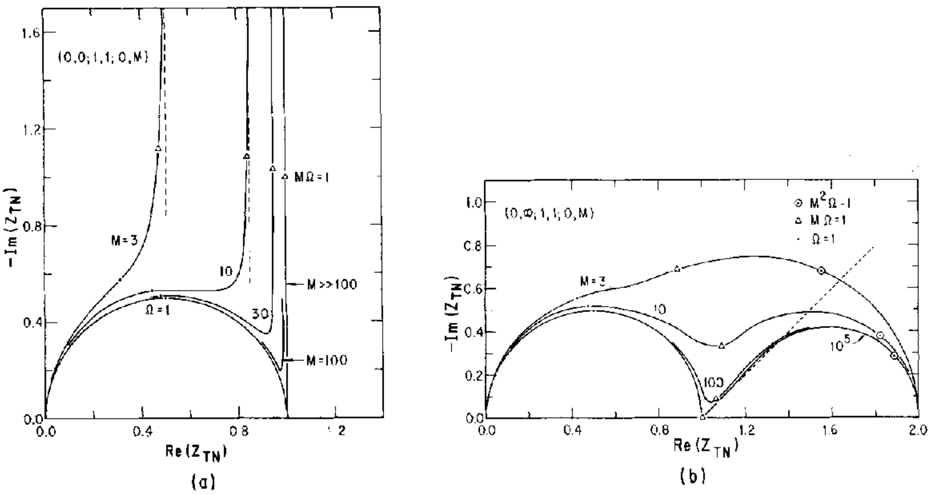

Fig. 3. Impedance-plane plots of normalized impedance components for (0, 0; 1, 1; 0, M) and (0, ∞; 1, 1; 0, M) situations and several M values.

Figure 3 shows how the size of M affects the shape of the curves for the two extreme cases (r_p, r_n)=(0, 0) and (0, ∞). Figure 3a indicates that in the completely blocking situation where $R_{EN}=1$ and $G_{DN}=0$, $Z_{TN} \cong 1+Z_{iN} \cong 1+(i\Omega C_{iN})^{-1}$ for $\Omega \lesssim M^{-1}$, and thus the reactance of the double-layer capacitance dominates in this region. Alternatively, when $\Omega > 0.1$ and $M > 10^2$, $Z_{TN} \cong Z_{3N}$. Note that in terms of Z_T rather than Z_{TN}, the semicircle lies between Re(Z_T)=0 at $\Omega \to \infty$ and Re(Z_T)=R_∞ at $\Omega \sim 0.1$.

Figure 3b shows that in the usual case of $M > 10^2$, two connected arcs appear for (0, ∞; 1, 1; 0, M), while they become merged as M decreases towards zero. Here for large M and $\Omega \gtrsim M^{-1}$, only the Debye dielectric relaxation semicircle appears. In the opposite extreme, as $\Omega \to 0$, $Z_{TN} \to Z_{TN0}$. Since $|Z_{iN0}|=\infty$, eqn. (3) shows that $Z_{TN0}=R_{DN}$. Whenever both r_p and r_n are not simultaneously zero, R_{DN} is finite. Here, in the equal mobility case, $R_{DN}=\varepsilon_n^{-1}=1+\pi_m^{-1}=2$. Further detailed consideration of circle diagrams and other response curves for the equal-mobility cases (0, 0; 1, 1; 0, M) and (0, ∞; 1, 1; 0, M) has been given earlier[2,3].

The dashed line in Fig. 3b through the point (1, 0) is drawn with a slope of 45 degrees. Where the second arc is well approximated by this line, Re(Z_{TN}) $\cong 1+$

$[-\mathrm{Im}(Z_{TN})]$. But this is just the result one finds when a Warburg impedance is in series with a bulk resistance R_∞. Thus, such a straight line segment of an arc in the impedance plane may be (and usually is) an indication of Warburg behavior, although it is also necessary that the Warburg part of the impedance be proportional to $\omega^{-\frac{1}{2}}$. Such behavior will be considered in much more detail later. It appears when diffusion to an electrode of mobile entities influences cell behavior appreciably.

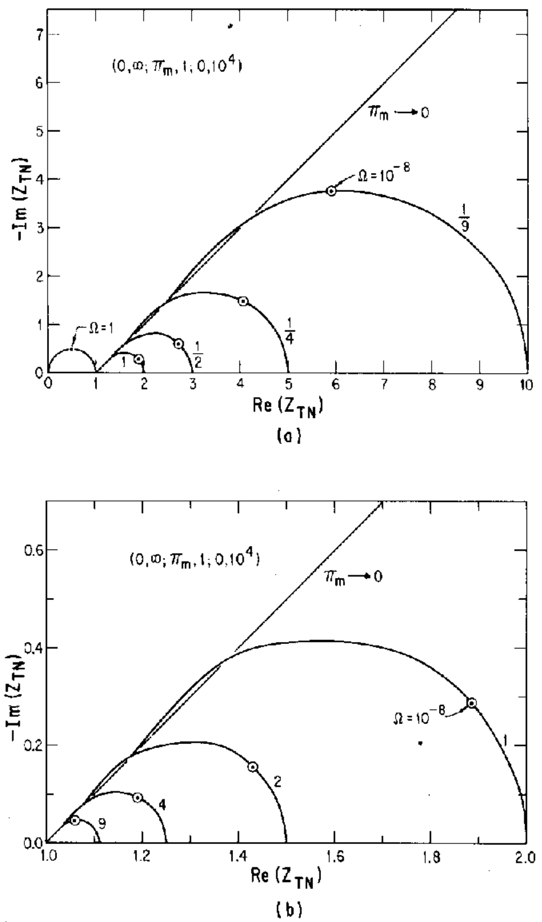

Fig. 4. Impedance-plane plots for $(0, \infty; \pi_m, 1; 0, 10^4)$ situations with $\pi_m \gtrless 1$. The $0 \leqslant \mathrm{Re}(Z_{TN}) < 1$ region has been omitted from the bottom plot.

Figure 4 shows circle diagram results for $(0, \infty; \pi_m, 1; 0, 10^4)$. π_m variation for $(0, 0; \pi_m, 1; 0, M)$ has relatively little effect here, but this is clearly not the case when both charges are not blocked. Further, π_z values different from unity within the range $0.25 \leqslant \pi_z \leqslant 4$ set by available ionic valences make little difference in the shapes of the arcs of Figs. 3–6; significant effects of π_z variation will be demonstrated later for some other types of plots. Note the different scales used for the two parts of Fig. 4. In addition, the $\Omega > 0.1$ semicircle has been omitted from

Fig. 4b for simplicity. Also, the line marked $\pi_m \to 0$ in Fig. 4a and 4b is the limit curve that the arc approaches as π_m approaches zero, not the actual limit when $\pi_m = 0$. There is a discontinuity in shape between curves for π_m arbitrarily small but non-zero (R_{DN} finite) and that for $\pi_m = 0$ (R_{DN} infinite). In the latter case, the charge carrier which is free to discharge has no mobility and therefore cannot discharge. Thus, the cases $(0, \infty; 0, \pi_z; 0, M)$ and $(0, 0; 0, \pi_z; 0, M)$ must lead to exactly the same results, as is indeed found. Finally, note that when the discharging carrier has much higher mobility than the blocked one, *e.g.* the $\pi_m = 9$ curve of Fig. 4b, the right-hand arc is very small compared to the dielectric relaxation semicircle. Thus, for such cases as $(0, \infty; \pi_m, \pi_z; 0, M)$ with $\pi_m \gg 1$, it will be difficult to subtract out the dominating effect of dielectric relaxation and obtain accurately the small remaining effects arising from electrode processes. As we shall see later, this is a low Q (Q = quality factor) and high dissipation factor situation.

Figure 5 shows how the shape of the circle diagram depends on r_p when $r_n = \infty$ and on r_n when $r_p = 0$ for the $\pi_m = \pi_z = 1$ case. Only part of the dielectric relaxation semicircle has been shown in Fig. 5a. Note that the heights of the arcs at the right are here proportional to $(1 + r_p)^{-1}$. The curves of Fig. 5b are interesting since they exhibit a total of three connected arcs when $r_n < \infty$. Clearly, the size of the middle arc depends directly on r_n. Further, the middle arc remains coincident with a semicircle over most of its extent, indicating a second single-time-constant Debye

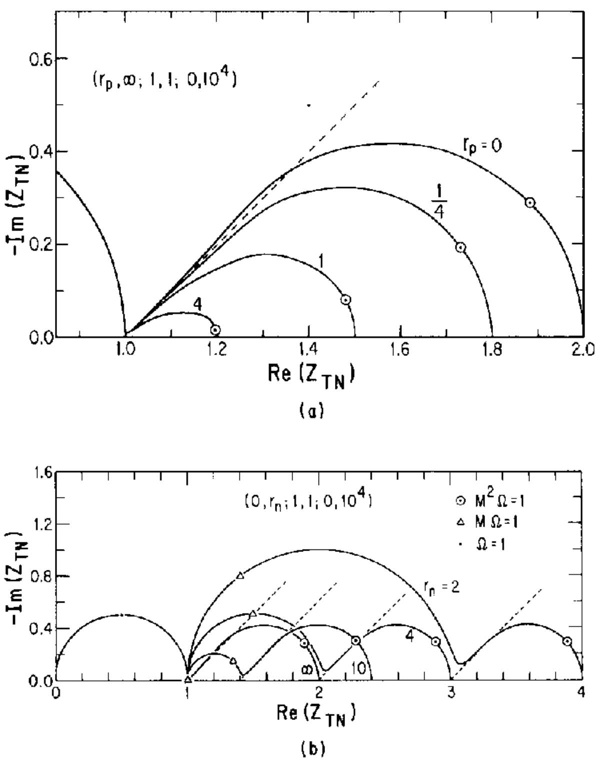

Fig. 5. Impedance-plane plots for the $(r_p, \infty; 1, 1; 0, 10^4)$ and $(0, r_n; 1, 1; 0, 10^4)$ situations.

dispersion in this region with a time constant dependent on r_n. Clearly, if frequency response measurements aren't extended to sufficiently high frequencies and if R_∞ and C_g are unknown, this middle semicircle might possibly be mistaken for the final $\Omega > 0.1$ semicircle. The low-frequency arc meets the $\mathrm{Re}(Z_{TN})$ axis at the low-frequency-limiting value of R_{DN}. Here, $R_{DN} = \varepsilon_n^{-1}[1+(2/r_n)] = 2[1+(2/r_n)]$. Further, the cusp at the beginning of this arc occurs at approximately $\mathrm{Re}(Z_{TN}) = [1+(2/\varepsilon_n r_n)]$. Thus, the radius of the middle semicircle is $(\varepsilon_n r_n)^{-1}$, here equal to $(2/r_n)$.

Although Fig. 5a shows that as r_p becomes larger the low-frequency arc becomes smaller and smaller relative to the Z_{3N} semicircle, and thus electrode processes become more and more difficult to isolate, this trend may be counteracted, provided r_p is not too large, by the presence of a sufficiently small π_m ratio. The curves of Fig. 6 show results for $\pi_m = 9^{-1}$, $r_n = 2$, and r_p variable. Again, three arcs appear with at least one very large compared to the dielectric relaxation semicircle. The very rapid reduction of the sizes of the two lower frequency arcs of Fig. 6 as r_p increases from zero arises primarily from the very strong dependence of G_{DN} on r_p, especially when $\pi_m \ll 1$, not so much from changes of Z_{iN} with r_p. When three arcs are present, they will be numbered from right to left in order of increasing frequency: 1,2,3. When an arc such as No. 2 is missing, the remaining arcs will maintain their original numbers: 1 and 3.

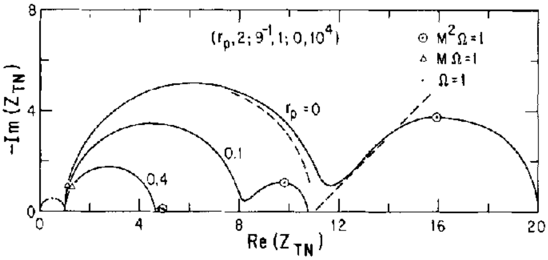

Fig. 6. Impedance-plane plot for the $(r_p, 2; 9^{-1}, 1; 0, 10^4)$ situation.

The sizes of the three normalized arcs which appear when $0 \leq r_p < r_n < \infty$ are of particular interest since many experimental results show two or three arcs of the present types. Frequently, the dielectric relaxation semicircle (arc No. 3) either has not been measured or is much smaller than the other two arcs. It is often found that the low-frequency right arc is much larger than the middle semicircle and, in many cases, measurements are not extended to sufficiently low frequencies to allow much curvature in the right arc to show up. Then only an approximately straight line often at about a 45° slope appears. In this case, measurements remain in the approximate Warburg frequency response region and do not approach the low-frequency saturation region. It is worth mentioning that some authors[13,14], working with glass membrane electrodes, have observed arcs 1 and 3 (or more probably 2 and 3) and have ascribed the higher frequency arc to the basic material under investigation and the lower frequency arc to a hydrolyzed surface film on the material. The present results show that such an assumption is unnecessary and that a single homogeneous material can yield both arcs.

Let us now consider the important three-arc $(0, r_n; \pi_m, \pi_z; 0, M)$ situation.

It turns out that an approximate expression for $Z_{TN}(\Omega)$ can be obtained which extends eqn. (4) to lower frequencies and includes separate terms for each of the three possible arcs, thereby partitioning Z_{TN} into three normalized impedances frequently dominant in different frequency regions. An exact partition of this type has already been presented in the two-arc $(0, \infty;\ 1,\ 1;\ 0,\ M)$ situation[3]. The approximate relation applying in the present case is, for $M \gtrsim 10$,

$$Z_{TN} \cong \sum_{j=1}^{3} Z_{jN} \tag{4'}$$

where

$$Z_{1N} \equiv t^2[t^2\pi_m\gamma_2 + i\Omega\{(\delta_p/\varepsilon_p)^2(r-1)+1\}] \equiv [G_{1N}+i\Omega C_{1N}]^{-1} \tag{4''}$$

and

$$Z_{jN} \equiv [G_{jN}+i\Omega C_{jN}]^{-1} \qquad (j=2,3) \tag{4'''}$$

Here, $\gamma_2 \equiv (ibM^2\Omega)^{\frac{1}{2}} \coth (ibM^2\Omega)^{\frac{1}{2}}$; $b \equiv \delta_n\delta_p/\varepsilon_n\varepsilon_p$; $t \equiv (1+i\Omega)^{\frac{1}{2}}$; $G_{2N} \equiv (\varepsilon_n r_n/2)$; $C_{2N} \equiv r \cong M$; $G_{3N}=1$; and $C_{3N}=1$. Equation (4′) is exact for $(0, \infty;\ \pi_m,\ \pi_z=\pi_m;\ 0,\ M)$, and in other cases is most accurate when $b\Omega \ll 1$. It may be further simplified, with little loss of accuracy, by taking $t=1$ for all Ω.

The partition represented by eqn. (4′) leads directly to an approximate equivalent circuit made up of three parallel GC sections in series when $0<r_n<\infty$. The quantity Z_{2N} is zero when $r_n=\infty$, causing arc 2 to disappear. Although Z_{1N} may be represented either as a frequency-dependent resistance in series with a frequency-dependent capacitance or as a conductance and capacitance in parallel, the parallel representation is best in the low frequency saturation region because it makes it clear that $\mathrm{Re}(Z_{TN0})$ is overtly finite, as it should be when r_p and r_n are not both zero. For $\Omega \to 0$, eqns. (4′), (4″), and (4‴) lead to the exact result $Z_{TN} \to Z_{TN0} = R_{1N}+R_{2N}+R_{3N} = \pi_m^{-1}+(2/\varepsilon_n r_n)+1 = \varepsilon_n^{-1}[1+(2/r_n)] \equiv R_{DN}$. When $\Omega > 10(bM^2)^{-1}$, Z_{1N} shows approximate Warburg frequency response, while G_{1N} and C_{1N} approach their low-frequency-limiting values for $\Omega < 2.5(bM^2)^{-1}$. Note that Z_{2N} is independent of π_z, and Z_{1N} depends on it primarily through b, a quantity symmetric in δ_n and δ_p. Incidentally, although eqn. (4′) holds approximately even for $r_n=0$, it can be considerably improved for this situation by multiplying Z_{1N} by δ_n^2 when $r_n=0$ and π_m is appreciably less than unity. This factor is otherwise inappropriate, however.

The expression for the second semicircle (arc 2) is particularly interesting. Here, $C_2 \cong MC_g$ is just the ordinary double-layer capacitance when $M \gg 1$ and $r_p=r_n=0$. This does not mean, however, that either C_p or C_i is equal to C_2 over the full frequency range where this semicircle is dominant. When $\pi_m=1$, neither C_p nor C_i remains near MC_g over an appreciable frequency region, even though the impedance-plane shape is well approximated by a semicircle. When $\pi_m \ll 1$, on the other hand, C_{iN} decreases to approximately M and then remains near it over an appreciable region, especially when $r_n \ll M$. It further turns out that C_{PN} reaches M at a lower Ω value than does C_{iN} and then remains near M while C_{iN} does. The maximum of this semicircle is $-\mathrm{Im}(Z_{2N})=(\varepsilon_n r_n)^{-1}$ and occurs at $\Omega=(\varepsilon_n r_n/2M)$. Clearly, $(\varepsilon_n r_n)^{-1}$ may greatly exceed 0.5, the maximum of arc 3. Under some conditions, such as $r_p=r_n\equiv r_e$, arc 1 is completely missing and only arcs 2 and 3 appear. In other possible conditions, arc 1 is so much smaller in size than arc 2 that it can be entirely neglected.

The quantity Z_{1N} yields the right arc (arc 1), which always appears to some degree, as in Figs. 3b, 4, 5 and 6, when $0 \leqslant r_p < r_n$. To good accuracy, the size and shape of this arc is entirely independent of r_n when $0 \leqslant r_p \ll 2\varepsilon_n$. Then the maximum value of $-\mathrm{Im}(Z_{1N})$ is about 0.417 π_m^{-1}, occurring at $\Omega \cong 2.53\ b^{-1}\ M^{-2}$. For $\pi_z = 1$ and $\pi_m \ll 1$, this value of Ω is about $10\ \pi_m M^{-2}$. When appreciable portions of all three arcs can be observed and they are distinct, one may very readily derive values of the pertinent parameters in the $(0, r_n; \pi_m, \pi_z; 0, M)$ situation. First, R_∞ is found from the cusp between arcs 2 and 3. Then C_g may be obtained at high enough frequencies that some appreciable portion of arc 3 appears. The Ω scale is then determined. Next, π_m may be obtained from the maximum height of arc 1. The high point on arc 2 then yields r_n (since ε_n and ε_p may be calculated from the value of π_m), and the Ω value at which this maximum occurs, $\Omega = \varepsilon_n r_n / 2M$, yields M. If the $\Omega \rightarrow 0$ intercept of arc 1 can be obtained, the resulting value of R_{DN} will then yield a check on the consistency of the previously found values of ε_n and r_n. Only π_z is missing. It will frequently be known from the physical situation being investigated; if not, an estimate may be obtained from a detailed comparison of the shape and frequency dependence of arc 1, using eqn. (4″).

Finally, note that even when $r_p = 0$ and $r_n < \infty$, there are combinations of π_m, π_z, and M values which lead to some melding of the three arcs so that the cusps between them may become less sharp and even disappear. Although the curves of Figs. 3–6 and eqn. (4′) have by no means illustrated all possible circle diagram shapes inherent in the theory, they should give some idea of the variety possible. One, two, or three connected arcs of different relative sizes follow from the theory. Probably even more than three would appear if charge types with more than two different mobilities were present.

It is hoped to show in a future paper under what conditions a more accurate but still simple version of eqn. (4′), may be derived from the exact theory; to show how accurate eqn. (4′) and its generalizations are for further cases of interest; and to demonstrate a wider variety of two-and-three arc shapes following from the theory. Since the present eqn. (4′) holds, however, within better than one percent under many r_n, π_m, π_z conditions when $b\Omega \ll 1$, it may already be used for experimental analysis when $r_p = 0$.

In the present part of this section, we have dealt with the approximate relation $Z_{TN} \cong Z_{1N} + Z_{2N} + Z_{3N}$, which does not involve the "interface" impedance Z_i directly. For the remainder of this paper, we shall instead pursue the more accurate and general approach of considering the exact equivalent circuit of Fig. 1 and the quantity Z_{iN}, which has been given exactly in closed form[4] and may be calculated without approximation for the $(r_p, r_n; \pi_m, \pi_z; 0, M)$ situation.

Although a detailed comparison of the present possible impedance-plane curve shapes with experimental results will not be carried out here, they do seem sufficiently variable and complex to match quite well a considerable body of experimental shapes, *e.g.* many of those in refs. 13–17. It should be noted that frequently only a single arc is found, often of the shape of the low-frequency arc of Fig. 3b, Fig. 4, and Fig. 5a. This important shape, which is associated with diffusion, distributed circuit elements, and a finite, distributed-element transmission line, even appears for the input impedance of a bipolar transistor[18].

There will always be a Debye dielectric relaxation semicircle appearing at higher frequencies, but frequently either the diffusion arc size is so much larger than that of the $\Omega > 0.1$ semicircle (*e.g.*, $\pi_m \ll 1$ for $r_p \sim 0$, $r_n \sim \infty$) that the latter is completely overwhelmed and/or measurements cannot conveniently be extended to the region where $\Omega \gtrsim 0.1$ and the dielectric relaxation semicircle appears. Such extension is, of course, easier for a very high resistivity material where τ_D is large, and thus the ω for which $\Omega = 1$ occurs in the relatively low frequency range[13,14]. It should be noted that for (~ 0, $\sim \infty$; ~ 1, ~ 1; 0, M) when M is large the cusp between the two arcs (at $\mathrm{Re}(Z_{TN}) \cong 1$) represents a wide frequency range from $\Omega \sim M^{-1}$ to $\Omega \lesssim 0.1$. Over this range Z_{TN} varies very little and remains near unity. Although R_∞ may be found from this region, one must go to at least $\Omega \gtrsim 0.1$ to determine C_g accurately. Finally, it should be noted that sometimes four or more connected arcs appear experimentally and $\mathrm{Im}(Z_T)$ may even be positive[16]. The latter result is often ascribed to the presence of specific ionic adsorption.

TABLE 1

LOW-FREQUENCY LIMITING VALUES OF COMPONENTS OF Z_{iN} AND OF FREQUENCY-INDEPENDENT NORMALIZED CIRCUIT ELEMENTS

M	r_p	r_n	π_m	R_{iN0}	C_{iN0}	R_{EN}	R_{DN}
10^4	0	0	1	5×10^{-5}	9.999×10^3	1	∞
10^4	0	0	10^{-4}	2.500×10^3	9.999×10^3	1	∞
10^4	0	∞	1	7.995×10^{-1}	8.336×10^6	2	2
10^4	0	∞	10^{-4}	1.999×10^3	8.336×10^6	1.0001	1.0001×10^4
10^2	0	∞	10^{-4}	1.881×10^3	8.581×10^2	1.0001	1.0001×10^4
10^4	2	2	10^{-4}	4.9995×10^3	2.4998×10^3	2	2
10^4	0	2	10^{-4}	2.782×10^4	2.089×10^6	1.00005	2.0002×10^4
10^4	2	0	10^{-4}	4.782×10^4	2.089×10^6	1.9998	2.0002
10^4	2	∞	10^{-4}	7.997×10^3	2.084×10^6	2.0002	1.9998

IV. IMPEDANCE FREQUENCY RESPONSE

Figures 7–11 show how the real and imaginary parts of Z_{TN} and Z_{iN} depend on frequency for various cases of interest. In addition, Table 1 gives values for pertinent circuit quantities for the various cases considered in this section. Although an Ω scale is given at the top of Figs. 7a and 8a, the main frequency variable used here is Λ^{-1}, where the diffusion related[3] quantity Λ is given by $M\Omega^{\frac{1}{2}}$. Note that when $M = 10^4$, the points $\Omega = 1$, $M\Omega = 1$, and $M^2\Omega = 1$ occur at $\Lambda^{-1} = 10^{-4}$, 10^{-2}, and 1, respectively. The use of a frequency variable proportional to $\omega^{-\frac{1}{2}}$ is common in electrochemical studies and immediately shows up the presence of Warburg behavior.

Let us write a general Warburg impedance Z_W as

$$Z_W \equiv A_0(1-i)/\omega^{\frac{1}{2}} \tag{5}$$

where the constant A_0 will be considered in detail in Section V. Then in normalized terms one has

$$Z_{WN} \equiv Z_W/R_\infty = A(1-i)/\Omega^{\frac{1}{2}} \tag{6}$$

where

$$\begin{aligned} \Lambda &\equiv (C_g/R_\infty)^{\frac{1}{2}} A_0 \\ &= [\varepsilon e(z_p p_i + z_n n_i)(\mu_p + \mu_n)/8\pi l^2]^{\frac{1}{2}} A_0 \end{aligned} \tag{7}$$

Now when the real part of a normalized impedance is the negative of its imaginary part and both depend on $\Omega^{-\frac{1}{2}}$, then the impedance in question exhibits Warburg behavior. In this case, both quantities will show a slope of unity, as in Fig. 8b, when plotted *versus* Λ^{-1}. On the other hand, when a capacitative reactance involves a frequency-independent capacitance, plotting *versus* Λ^{-1} will yield a straight line with a slope of two as in Fig. 7a.

Figure 7 shows results for the completely blocking case for two different π_m conditions. Here eqn. (3) yields

$$Z_{TN} = (Z_{iN} + 1)/[1 + i\Omega(Z_{iN} + 1)] \tag{8}$$

Now computer calculations indicate that for the equal-mobility case shown in Fig. 7a, $C_{iN} = C_{iN0} \equiv r - 1 \cong M$ within 1 percent up to $\Omega \cong 0.3$. Further, the Figure shows that $\text{Re}(Z_{iN}) \equiv R_{iN}$ remains very near its small limiting value[4] of $R_{iN0} = (2M)^{-1}$ up to $\Omega = 1$. Thus, in the entire frequency range of interest, we may here take $Z_{iN} \cong Z_{iN0}$ and, further, may neglect R_{iN0} and C_{iN0}^{-1} compared to unity. Then (8) leads to

$$Z_{TN} \cong \{1 - i[\Omega + (M\Omega)^{-1}]\}/(1 + \Omega^2) \tag{9}$$

Clearly, for $M\Omega \ll 1$ ($\Lambda^{-1} \gg 10^{-2}$), the normalized capacitative reactance $(\Omega C_{iN})^{-1} \cong (\Omega C_{iN0})^{-1} \cong (M\Omega)^{-1}$ dominates Z_{TN}. Further consideration of this case has been presented earlier[1–3].

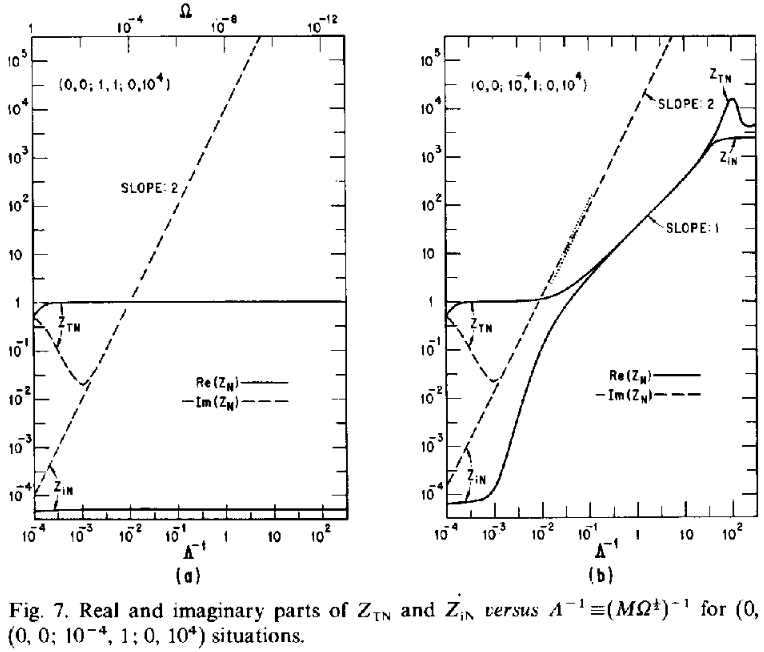

Fig. 7. Real and imaginary parts of Z_{TN} and Z_{iN} *versus* $\Lambda^{-1} \equiv (M\Omega^{\frac{1}{2}})^{-1}$ for (0, 0; 1, 1; 0, 10^4) and (0, 0; 10^{-4}, 1; 0, 10^4) situations.

Although Fig. 7b shows that in the $\pi_m \ll 1$ case, $\mathrm{Im}(Z_{iN})$ still dominates Z_{TN} for $M\Omega \ll 1$, there is evident a transition from $C_{iN} \cong C_{iN0}$ to a smaller constant value, C_{isN}, in the neighborhood of $\Lambda^{-1} \cong 4 \times 10^{-2}$. This plateau value, C_{isN}, will be discussed in detail in the next Section. Figure 7b also indicates that R_{iN} is much larger and more frequency dependent than it is when $\pi_m = 1$. Note that although $\mathrm{Re}(Z_{TN})$ and R_{iN} show an appreciable region with a slope of unity, this does not indicate pure external Warburg behavior since the dominant normalized reactances show no such slope. Warburg behavior actually occurs here in both $\mathrm{Re}(Z_{TN})$ and $\mathrm{Im}(Z_{TN})$, as shown by eqn. (4′) with $r_p = r_n = 0$, but its contribution to $\mathrm{Im}(Z_{TN})$ is swamped by the reactance of C_{iN0} and C_{isN}. Finally, note that the components of Z_{TN} are essentially exactly the same for $\pi_m = 1$ and 10^{-4} when $\Omega \gtrsim 10^{-2}$ ($\Lambda^{-1} \lesssim 10^{-3}$). Thus, the mobility ratio has very little effect in this relatively high frequency region.

Next we turn to the $(0, \infty)$ case. For the $\pi_m = 1$ situation of Fig. 8a, eqn. (3) yields

$$Z_{TN} = \frac{(Z_{iN} + 2)}{1 + (i\Omega + 0.5)(Z_{iN} + 2)} \tag{10}$$

When $\Omega \ll 1$ and $|Z_{iN}| \ll 4$, this result reduces to

$$Z_{TN} \cong 1 + (Z_{iN}/4) \tag{11}$$

In the region $10^{-2} \lesssim \Lambda^{-1} \lesssim 10^{-1}$, the unity slope $-\mathrm{Im}(Z_{TN})$ and $-\mathrm{Im}(Z_{iN})$ lines of Fig. 8a are separated by just this factor of four.

The most interesting aspect of Fig. 8a is the Warburg behavior of Z_{iN} in the region $10^{-3} \lesssim \Lambda^{-1} \lesssim 10^{-1}$. Such behavior does not show up directly here in

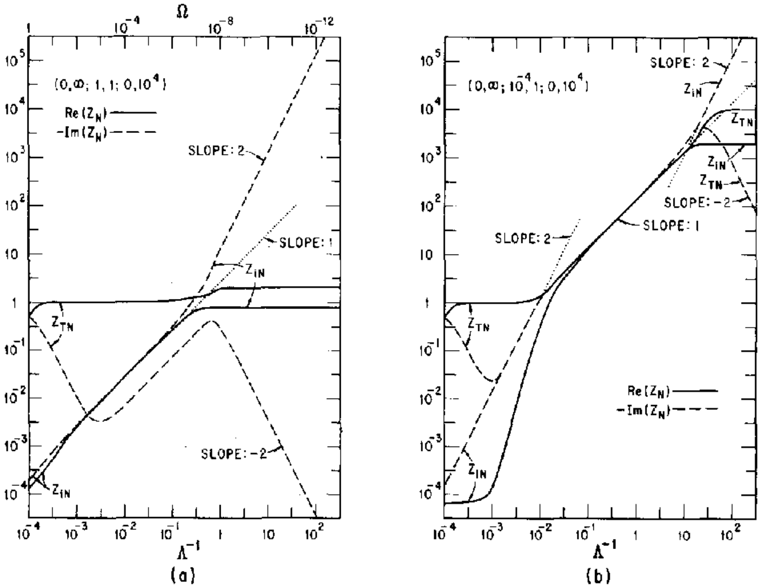

Fig. 8. Real and imaginary parts of Z_{TN} and Z_{iN} *versus* Λ^{-1} for $(0, \infty;\ 1,\ 1;\ 0,\ 10^4)$ and $(0, \infty;\ 10^{-4},\ 1;\ 0,\ 10^4)$ situations.

$\mathrm{Re}(Z_{TN})$ because of the overlying effects of R_{EN} and R_{DN}. It is only when these effects are eliminated by calculating Z_{iN} from (10), or minimized, by calculating it from (11), that Warburg sort of behavior shows up clearly. Relatively small deviations from exact Warburg behavior of Z_{iN} are of particular interest and will be examined in depth in Section VI.

It is especially important to note that basic Warburg behavior appears in the Z_{iN} normalized "interface" impedance, not necessarily directly in Z_{TN}. If in the equal-mobilities case $(Z_T - R_\infty)$ is set directly equal to a theoretical Warburg impedance in the usual way, rather than to such an impedance divided by 4, a factor of four error can occur, for example, in the calculation of the concentration of the charge involved in the Warburg behavior. Even greater errors can occur for $\pi_m > 1$, and lesser ones will appear for $\pi_m < 1$. Note that even in the present $\pi_m = 1$ case, a small difference, $\mathrm{Re}(Z_{iN}/4)$, between two much larger quantities must be calculated to obtain the real part of the Warburg response. Experimental errors are thus magnified and make it difficult to obtain Z_{iN} accurately from Z_{TN} when $\pi_m \gtrsim 1$.

The situation is considerably different when $\pi_m \ll 1$, as in Fig. 8b. Here approximate Warburg response shows up in both Z_{TN} and Z_{iN} in the region $0.03 \lesssim \Lambda^{-1} \lesssim 10$. Here eqn. (3) yields

$$Z_{TN} \cong \frac{(Z_{iN}+1)}{1+(i\Omega+\pi_m)(Z_{iN}+1)} \tag{12}$$

which for the present $\pi_m = 10^{-4}$ and the range $10^{-10} \lesssim \Omega \leqslant 10^{-2}$, becomes

$$Z_{TN} \cong Z_{iN} + 1 \tag{13}$$

Thus, in the $\pi_m \ll 1$ region, no error such as that of a factor of 4 just discussed for the $\pi_m = 1$ case appears when the conventional procedure is used. Incidentally, the distinction between Z_{iN} and $(Z_{iN}+1)$ is not visible on the present log–log plot for $\Lambda^{-1} > 0.1$. The final low-frequency-limiting values of $\mathrm{Re}(Z_{TN})$, R_{DN}, and $\mathrm{Re}(Z_{iN})$, R_{iN0}, are given in Table 1.

In Fig. 9 the same case as that of Fig. 8b is considered except that $M = 10^2$ rather than 10^4. Note that the results are essentially the same near and in the low-frequency saturation region, $\Lambda^{-1} \gtrsim 10$. The vestiges of Warburg behavior still appear for $3 < \Lambda^{-1} \lesssim 10$ but do not extend very far toward higher frequencies. Here the conditions $\Omega = 1$, $M\Omega = 1$, and $M^2\Omega = 1$ occur at $\Lambda^{-1} = 10^{-2}$, 10^{-1}, and 1, respectively. The very high frequency $\Lambda^{-1} < 10^{-2}$ region is shown here for completeness but will generally not be experimentally accessible since the impedance level at say $\Lambda^{-1} \sim 10^{-3}$ or 10^{-4} is so much lower than that in the low-frequency saturation region and than R_∞. Thus, the second Warburg response region of Z_{iN}, occurring[2] at $\Lambda^{-1} < 10^{-2}$, will not usually be measurable. This region appears for any π_m and reasonably large M for $\Omega > 1$ but has been omitted from the other plots for simplicity.

Finally, Figs. 10 and 11 show the curves which appear for a few related choices of r_p and r_n. Note that the value r_p or $r_n = 2$ makes g_p or $g_n = 2$ rather than its unity value when r_p or $r_n = 0$. It is the g's rather than the r's which enter directly into the theory; thus r_p and r_n values which double g seem reasonable to choose for special examination. The results of Fig. 10a should be compared especially with those of 7b and 8b. Similarly, Fig. 10b should be

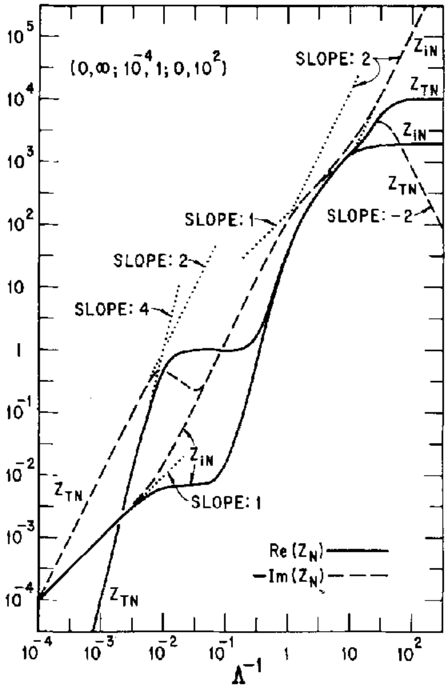

Fig. 9. Real and imaginary parts of Z_{TN} and Z_{iN} *versus* Λ^{-1} for (0, ∞; 10^{-4}, 1; 0, 10^2) showing the effect of a reduction in M.

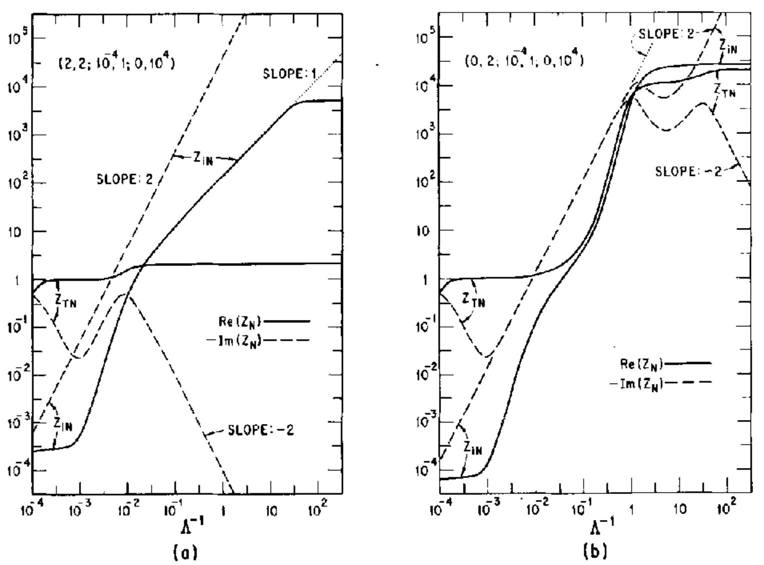

Fig. 10. Real and imaginary parts of Z_{TN} and Z_{iN} *versus* Λ^{-1} for (2, 2; 10^{-4}, 1; 0, 10^4) and (0, 2; 10^{-4}, 1; 0, 10^4) situations.

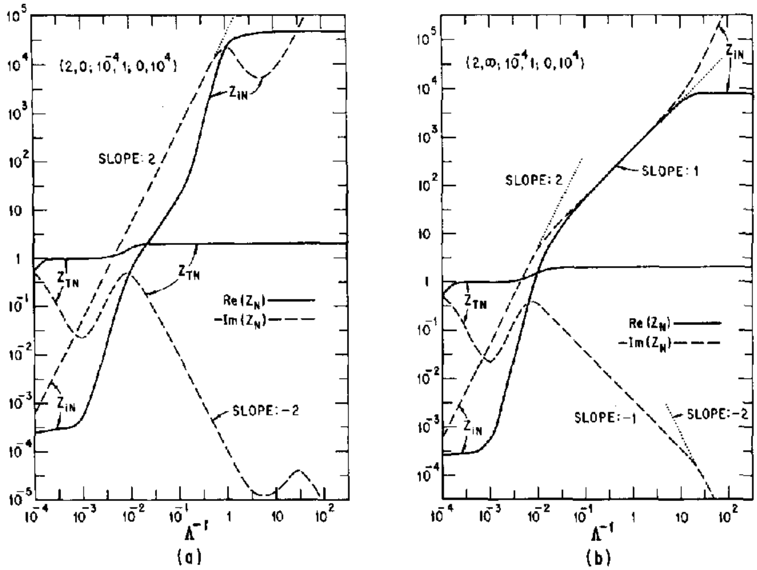

Fig. 11. Real and imaginary parts of Z_{TN} and Z_{iN} *versus* Λ^{-1} for (2, 0; 10^{-4}, 1; 0, 10^4) and (2, ∞; 10^{-4}, 1; 0, 10^4) situations.

compared with Figs. 10a, and 8b. Note that the double hump in the $-\mathrm{Im}(Z_{TN})$ curve of Fig. 10b is associated with the Z_{2N} and Z_{1N} terms of eqn. (4′); thus, in this situation an impedance-plane plot would show three connected arcs, although the dielectric relaxation one will be far smaller than the other two here. The results of Fig. 11a should be compared with 10a and those of 11b with 11a, 8a, and 8b. It will be seen that the change of a single blocking parameter from 0 to 2 or 2 to ∞ can make a great deal of difference in some or all of the curves. Further, no approximate Warburg regions occur here except for the (2,∞; 10^{-4}, 1; 0, 10^4) case of Fig. 11b which is clearly not too far different from (0, ∞; 10^{-4}, 1; 0, 10^4) as far as Z_{iN} is concerned, although even here the normalized impedance level is higher. Here, however, Z_{TN} and Z_{iN} are again connected very closely by eqn. (10), which does not reduce to $Z_{TN}=(Z_{iN}/4)+1$ or $(Z_{iN}+1)$ in the region of interest.

Solution of eqn. (3) for Z_{iN} yields

$$Z_{iN} = \frac{Z_{TN}}{1-(i\Omega+G_{DN})Z_{TN}} - R_{EN} \tag{14}$$

When $i\Omega$ may be neglected, this result reduces to[3]

$$\begin{aligned} Z_{iN} &\cong R_{EN}^2[Z_{TN}-1]/[1-G_{DN}R_{EN}(Z_{TN}-1)] \\ &= R_{EN}[Z_{TN}-1]/[1-G_{DN}Z_{TN}] \end{aligned} \tag{15}$$

In the $\Lambda^{-1} \gtrsim 10^{-1}$ region, where $Z_{TN} \cong R_{DN}$, the denominator is nearly zero; thus again in the (2, ∞; 10^{-4}, 1; 0, 10^4) situation calculation of Warburg response from experimental Z_T results involves the small difference between two much larger quantities and will be difficult to obtain adequately. The present results allow us to conclude that for $M \gtrsim 10^2$ Warburg response will only be seen or be readily calculable when $r_p \ll 2$, $r_n \gg 2$, and most readily when $\pi_m \ll 1$. Of course one must also include the symmetry-related situation $r_p \gg 2$, $r_n \ll 2$, and $\pi_m \gg 1$.

V. FREQUENCY RESPONSE OF THE ADMITTANCE COMPONENTS

Equation (3) may be readily inverted to yield a connection between Y_{TN} and the elements of Z_{iN}. Let $R_{SN} \equiv R_{iN} + R_{EN}$, the total normalized series resistance in the bottom branch of Fig. 1a. Further, let $\tau_{SN} \equiv R_S C_i/\tau_D \equiv R_{SN} C_{iN}$. Then $D_{SN} \equiv D_S = \Omega\tau_{SN} = \omega R_S C_i \equiv Q_S^{-1} \equiv \tan \delta_S$, where D_S is the dissipation factor and Q_S the quality factor for this branch. Similarly, we may define $\tau_{EN} \equiv R_{EN} C_{iN}$ and $D_E \equiv \Omega\tau_{EN}$. With these definitions eqn. (3) leads immediately to the important equations

$$C_{PN} = 1 + \frac{C_{iN}}{1+(\Omega\tau_{SN})^2} = 1 + \frac{C_{iN}}{1+D_S^2} \tag{16}$$

and

$$G_{PN} = G_{DN} + \frac{\Omega^2 \tau_{EN}\tau_{SN} G_{EN}}{1+(\Omega\tau_{SN})^2} = G_{DN} + \frac{D_E D_S G_{EN}}{1+D_S^2} \tag{17}$$

These equations, together with the frequency responses of R_{iN} and C_{iN}, yield those of C_{PN} and G_{PN} in complete generality. For $\Omega \to 0$, $C_{PN} \to C_{PN0} = 1 + C_{iN0}$ and $G_{PN} \to G_{PN0} = G_{DN}$. Note that we are here dealing with the components of the total admittance, *not* that after the effect of R_∞ or R_D and R_E is somehow subtracted out.

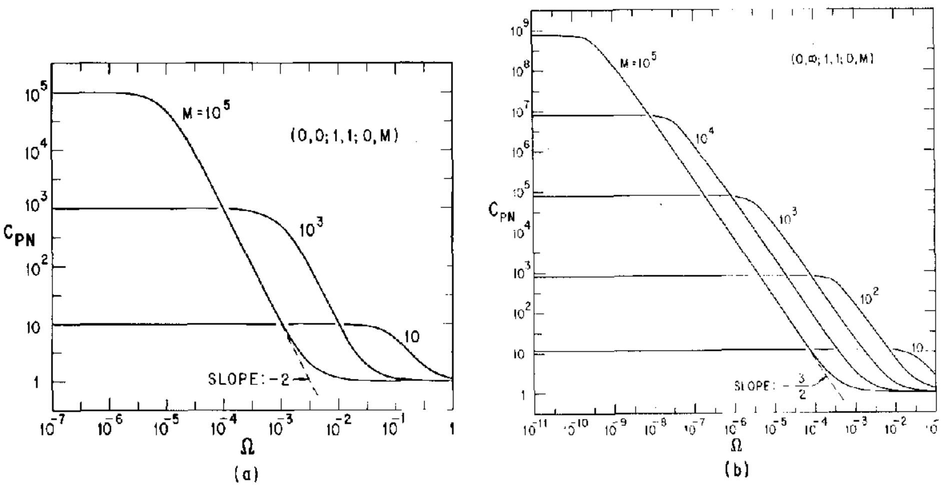

Fig. 12. C_{PN} *versus* Ω for $(0, 0; 1, 1; 0, M)$ and $(0, \infty; 1, 1; 0, M)$ situations and several M values.

Figure 12 shows how C_{PN} depends on Ω for various values of M in the $\pi_m = \pi_z = 1$ case. The curves of Fig. 12a follow nearly exactly from eqns. (16) and (17) with $C_{iN} = C_{iN0} \cong M-1$, $R_{iN} = R_{iN0} = (2M)^{-1}$ and $\tau_{SN} = (R_{iN0} + R_{EN})C_{iN0} \cong R_{EN} \times C_{iN0} \equiv \tau_{EN}$. Thus, one has simple Debye response here[1,19] with the only significant frequency response arising from those Ω's which appear overtly in (16) and (17). Incidentally, curves such as the $M=10^3$ ones of Fig. 12a and 12b have been observed[11] for F-centered KBr. One like that of Fig. 12a was indeed measured with completely blocking electrodes, while electrodes which were incompletely blocking to electrons yielded curves like those of 12b.

Figure 13 shows the frequency dependence of G_{PN} and C_{PN} when $r_p = r_n \equiv r_e$. In this equal-discharge case, eqn. (1) yields $C_{iN0} = (r-1)/g_e^2 \cong M/g_e^2$, where $g_e \equiv 1 + (r_e/2)$. For the present $\pi_m = \pi_z = 1$ situation, the corresponding R_{iN0} is approximately $g_e^2/2M$ and $R_{EN} = g_e$. These results, used in (16) and (17) with $C_{iN} = C_{iN0}$ and $R_{iN} = R_{iN0}$, again yield the curves of Fig. 13. Note that the $\Omega \to 0$ value of G_{PN} is here $G_{DN} = r_e/(2 + r_e)$. The low-frequency saturation value of C_{PN} is here reached for $\Omega \lesssim [g_e/10(r-1)]$.

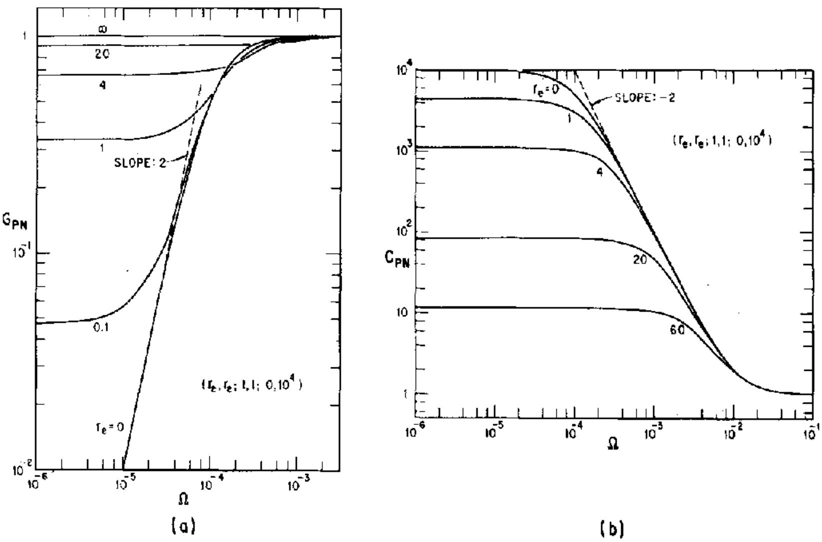

Fig. 13. Normalized frequency response of G_{PN} and C_{PN} for the $(r_e, r_e; 1, 1; 0, 10^4)$ situation.

Figure 14a shows some dependence on π_m and π_z for the completely blocking situation. Detailed calculations based on the earlier theoretical results[4] show that the plateau value of C_{iN}, C_{iSN}, is given in the present $\pi_m \leqslant 1$ situation by

$$C_{iSN} \cong (it_2 m_b/\Omega f_1 f_2) \cong [M\delta_p^{\frac{1}{2}} - 1]\varepsilon_p^{-1} \cong M\delta_p^{\frac{1}{2}} - 1 \tag{18}$$

where the quantities t_2, m_b, f_1, and f_2 are defined in the earlier work. The corresponding plateau value of C_{PN}, C_{PSN}, is, from (16), essentially $M\delta_p^{\frac{1}{2}}$ since $D_S \ll 1$ in the $C_{PN} \cong C_{PSN}$ plateau region. This region is limited approximately by $10\pi_m \lesssim \Omega \lesssim [10M\delta_p^{\frac{1}{2}}]^{-1}$ for $M \gtrsim 10^2$. Thus no such region appears unless $\pi_m \lesssim [10^2 M\delta_p^{\frac{1}{2}}]^{-1}$. Incidentally, C_{iN} remains at its plateau value over the larger range $10\pi_m \lesssim \Omega \lesssim 0.1$. Note that $M\delta_p^{\frac{1}{2}} = M2^{\frac{1}{2}} \cong 7071$ for $\pi_z = 1$ and $M5^{\frac{1}{2}} \cong 4472$ for $\pi_z = 4$, the two π_z values of Fig. 14a. Finally, the region where C_{PN} has essentially reached its low-frequency-limiting value C_{PN0} is given approximately by whichever of the following two conditions yields the minimum Ω: $\Omega \lesssim (10\,M)^{-1}$ and $\Omega(a-1) \ll 1$. Here $a \equiv (\delta_p^2/\varepsilon_p) + (\delta_n^2/\varepsilon_n)$, and for $\pi_z = 1$, $a = b$. The last Ω-condition above may be expressed more explicitly as $\Omega(a-1) \lesssim 2.5 \times 10^{-4}$. For $\pi_m = 10^{-6}$ and $\pi_z = 1$,

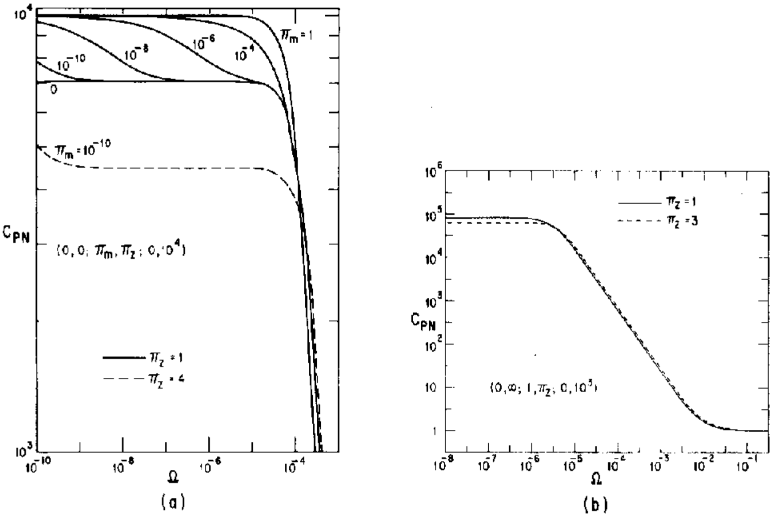

Fig. 14. Normalized frequency response of C_{PN} for $(0, 0; \pi_m, \pi_z; 0, 10^4)$ and $(0, \infty; 1, \pi_z; 0, 10^3)$ situations.

$a = b \cong 2.5 \times 10^5$, yielding $\Omega \lesssim 10^{-9}$ in the present case.

It is interesting to note that curves of very similar shape to the $\pi_z = 1$ curves of Fig. 14a were obtained long ago[19] for a $(0, 0; \infty, 1; 0, M)$ situation, one with charge of only one sign mobile but free to recombine with fixed charge of opposite sign. This is an idealization of conditions which might occur in a solid. Such generation-recombination essentially mobilizes the fixed charge[19, 20], and the time constant ratio $\xi^{-1} \equiv \tau_D/\tau_r$ of the earlier work[19] there plays the role of the present π_m mobility ratio. Here τ_r is a recombination time constant involving the bimolecular recombination rate constant k_2. Since $(0, 0; \infty, 1; 0, M)$ and $(0, 0; 0, 1; 0, M)$ situations lead to the same Z_{TN}, we may now consider the latter situation with recombination, since it closer corresponds to the present $(0, 0; \pi_m, 1; 0, M)$ situation with $\pi_m \ll 1$ and no recombination. The early work[19] indicates that the rise from C_{PSN} toward C_{PN0} begins at $\Omega = \Omega_r \cong 10\ \xi^{-1}$, while Fig. 14a shows the start at $\Omega = \Omega_m \cong 10\ \pi_m$. When $\Omega_m \gg \Omega_r$, or $\pi_m \gg \xi^{-1}$, the rise associated with motion of the lower mobility charge carrier occurs at a much higher frequency than that arising from recombination, and the presence or absence of the latter doesn't affect the frequency region where C_{PN} rises from C_{PSN} to C_{PN0}. On the other hand, when $\Omega_m \ll \Omega_r$ and $\pi_m \ll \xi^{-1}$, the recombination rise appears at the higher frequency, and it then doesn't matter how small the actual π_m is. Incidentally, for any substantial plateau to be possible it is necessary that Ω_r as well as Ω_m be appreciably less than M^{-1}. This requirement leads to $\xi \gg M$, or $\tau_r \gg M\tau_D$.

Since there will usually either be some small residual true mobility for the less mobile charge and/or some recombination when $\pi_m \equiv 0$ (this zero-mobility condition is never actually reached in solids at non-zero temperature), one should not[21] expect to find experimentally a curve corresponding all the way down to $\Omega = 0$ to that for $\pi_m = 0$ of Fig. 14a. At sufficiently low frequencies for non-zero temperature there will always be a transition from C_{PSN} to the larger C_{PN0}. This transition frequency may, however, be too low to determine conveniently experimentally. The above results justify the neglect of intrinsic recombination in the present theoretical analysis[4], although it should not be forgotten that non-zero recombination ($\tau_r < \infty$) affects the magnitudes of the equilibrium concentrations n_i and p_i directly in the present intrinsic conduction case. Thus, the presence of recombination also affects the value of M directly. As far as the normalized frequency response of Z_{TN} is concerned, however, recombination can be approximately accounted for by choosing and interpreting π_m properly. It is the effective mobility ratio that counts, that arising from both true mobility and from recombination. For practical purposes, the present π_m may thus be considered to represent the effective mobility ratio for any r_p, r_n situation. It will thus be the true π_m when $\pi_m \gg \xi^{-1}$ and will be ξ^{-1} when $\pi_m \ll \xi^{-1}$.

Before we leave the situation of only charge of a single sign mobile, it is instructive to compare the results of Beaumont and Jacobs[22], who considered the idealized $(-, \rho; \infty, 1; 0, M)$ situation without recombination [equivalent for Z_{TN} to $(\rho, -; 0, 1; 0, M)$ without recombination]. For the equivalent case, only the mobile positive charges discharge (with $r_p \equiv \rho$), and no r_n need be specified since the negative charges are taken immobile and homogeneously distributed. Beaumont and Jacobs' results for Z_{TN} turn out to be exactly the same as those which follow from the present treatment for $(r_e, r_e; \pi_m, \pi_z; 0, M)$ with $\pi_m = 0$ or ∞ and $\pi_z = 1$.

The $(r_e, r_e; 0, \pi_z; 0, M)$ situation leads, for example, to $C_{PN0} = C_{PSN} \cong g_e^{-2} M \delta_p^{\frac{1}{2}} + (1 - g_e^{-2})$. But, as eqn. (2) shows,

$$M\delta_p^{\frac{1}{2}} \equiv l\delta_p^{\frac{1}{2}}/2L_D = (l/2)[4\pi e^2 z_p^2 p_i/\varepsilon kT]^{\frac{1}{2}} \equiv l/2L_{Dp} \equiv M_p \tag{19}$$

where $L_{Dp} \equiv L_D/\delta_p^{\frac{1}{2}}$ is the Debye length which applies when only the positive carrier is mobile, the situation actually considered. In this case, Beaumont and Jacobs' results lead to $C_{PN0} = (M/2^{\frac{1}{2}})/[1 + (\rho/2)]^2$, in essential agreement with the present expression when $\pi_z = 1$. Further, their frequency response is of course the same as that found here.

The equivalence of these results again follows from the fact that it doesn't matter what boundary condition parameter one assigns to a charge carrier which is immobile. Thus, the g_e appearing in C_{PSN} is actually g_p in the $0 \leq \pi_m \ll M^{-1}$ case, and the value of r_n is immaterial. Further, eqn. (19) shows that in the present treatment it is unnecessary to deal with two separate Debye lengths, one defined where there is only one species of mobile carrier present and the other for two. The effect on formulas involving the Debye length of a shift from both positive and negative charge carriers mobile to only one type mobile occurs automatically here.

Figure 14b shows how C_{PN} depends on π_z for the $(0, \infty)$ discharge situation. On this scale the change from $\pi_z = 1$ to $\pi_z = 3$ is quite small. Incidentally, the $\pi_z = 3^{-1}$ curve lies so close to that for $\pi_z = 3$ that it cannot be shown separately on this plot. Although π_m has no effect on C_{PN0}, it does of course affect C_{PN} at non-zero Ω. Thus, it is possible to compensate the effect of $\pi_z \neq 1$ to large degree by choice of π_m, except in the neighborhood of low-frequency saturation. For example, the choice $\pi_m = 1.15$, $\pi_z = 3$, makes the resulting C_{PN} and G_{PN} curves lie almost exactly on those for $\pi_m = 1$, $\pi_z = 1$ except for the saturation region, $\Omega \lesssim 10\, \pi_m M^{-2}$. To illustrate, at $\Omega = 10^{-4}$, the $(0, \infty; \pi_m, \pi_z; 0, 10^3)$ case leads to the following values of C_{PN} for $(\pi_m, \pi_z)=(1, 3^{-1})$, $(1, 3)$, $(1, 1)$, and $(1.15, 3)$ respectively: 698.1, 695.4, 616.2, and 616.3. Corresponding values of G_{PN} are 0.9218, 0.9196, 0.9308, and 0.9300. This possible compensation effect requires one to be especially careful in deriving values of π_m and π_z from experiment in the rather unusual case where both ratios are initially unknown.

Figure 15 shows important results for G_{PN} and C_{PN} in the variable π_m discharge case. Notice that the C_{PN} curves show portions with slopes of -2, -1.5, and -0.5. The somewhat odd looking values of π_m used here result in $G_{PN0} \equiv G_{DN} = \varepsilon_n = (1+\pi_m^{-1})^{-1}$ yielding particularly simple values. The C_{PN} curves for $\pi_m \gg 9$ appearing in Fig. 15b are here included largely for completeness. As π_m increases, the resistance R_E in series with Z_i increase while R_D, in parallel with the Z_i, R_E branch, decreases toward R_∞. When $\pi_m = 999$, for example, $R_{DN} \cong 1.001$ and $R_{EN} = 10^3$. At $\Omega = 10^{-9}$, $R_{iN} \cong 134$ and $(\Omega C_{iN})^{-1} \cong 186$. Thus, as mentioned earlier, when $\pi_m \gg 1$, it will be difficult to obtain the components of Z_{iN} accurately.

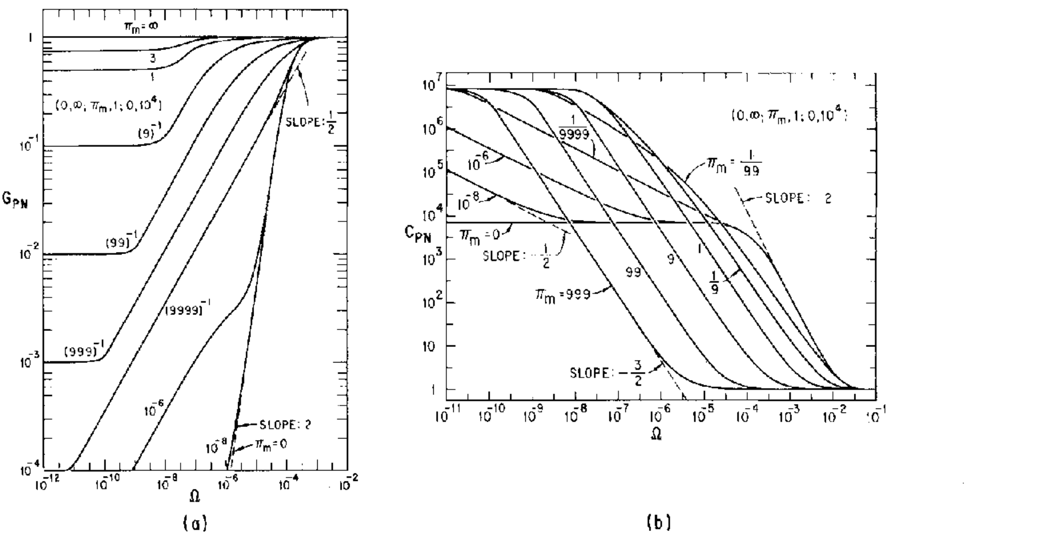

Fig. 15. Normalized frequency response of G_{PN} and C_{PN} for the $(0, \infty; \pi_m, 1; 0, 10^4)$ situation.

Let us now consider how the various types of curves of Fig. 15 may be explained. To do so, we need further information concerning $R_{iN}(\Omega)$ and $C_{iN}(\Omega)$. These quantities show approximate Warburg response in part of the Ω region and thus are approximately proportional to $\Omega^{-\frac{1}{2}}$ in this region. One way of showing such response is to plot the normalized quantities $C_{iD} \equiv A(C_{iN}/C_{iN0})$ and $R_{iD} \equiv A(R_{iN}/R_{iN0})$ *versus* Ω, as in Fig. 16. Those curves with slope 0.5 in Fig. 16a represent constant C_{iN} regions, that on the left for $C_{iN} \cong C_{iN0}$ and that on the right for $C_{iN} \cong C_{iSN}$, as will become clearer later. Similarly, the lines with slope 0.5 in Fig. 16b represent $R_{iN} \cong R_{iN0}$ regions while R_{iN} decreases as Ω^{-2} for the $\pi_m \leqslant 1$ lines with slope -1.5.

The regions with essentially zero slope in Fig. 16 are those where $Z_{iN} \cong Z_{WN}$. A more exact approximation for Z_{iN} in these regions will be considered in the next

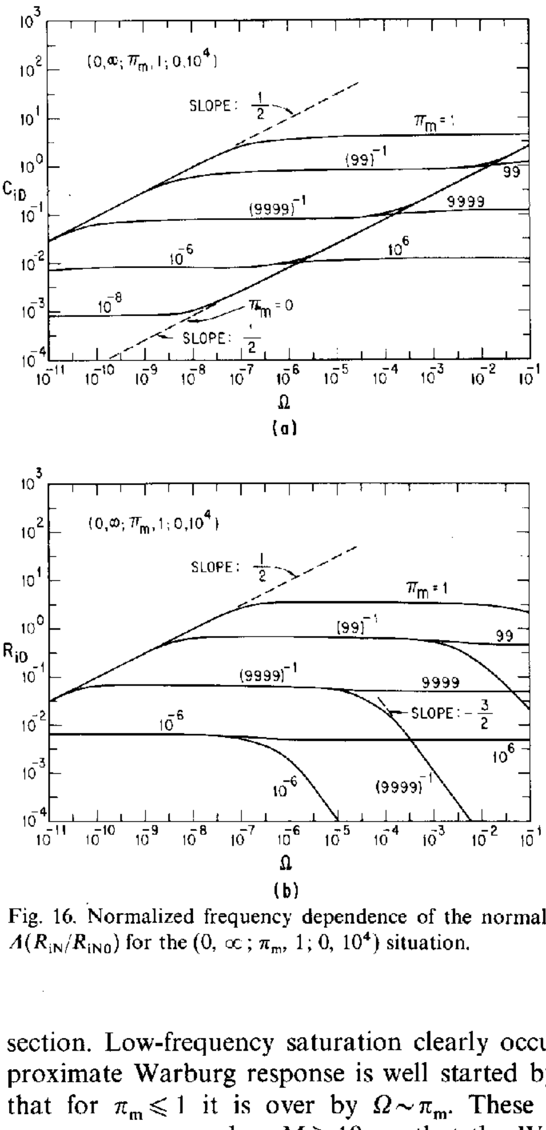

Fig. 16. Normalized frequency dependence of the normalized quantities $C_{iD} \equiv A(C_{iN}/C_{iN0})$ and $R_{iD} \equiv A(R_{iN}/R_{iN0})$ for the $(0, \infty; \pi_m, 1; 0, 10^4)$ situation.

section. Low-frequency saturation clearly occurs when $\Omega \lesssim 10\pi_m M^{-2}$. Thus, approximate Warburg response is well started by $\Omega \gtrsim 10^2\pi_m M^{-2}$. Figure 16 shows that for $\pi_m \leqslant 1$ it is over by $\Omega \sim \pi_m$. These results also indicate that no such response occurs unless $M \gtrsim 10$, so that the Warburg range is non-zero. We shall generally consider only $M \gtrsim 10^2$ from now on. Because the range of π_z is physically limited, the above Warburg range is still adequate for any experimental π_z, not just the $\pi_z = 1$ of Fig. 16, and the inequalities that limit it need not involve π_z.

In the Warburg range of Z_{iN}, we have approximately,

$$Z_{iN} \cong Z_{WN} \equiv R_{WSN} + (i\Omega C_{WSN})^{-1} \tag{20}$$

where

$$R_{WSN} \equiv A/\Omega^{\frac{1}{2}} \tag{21}$$

and

$$C_{WSN} \equiv (A\Omega^{\frac{1}{2}})^{-1} \tag{22}$$

Similarly, we may write

$$Y_{iN} \cong Y_{WN} \equiv Z_{WN}^{-1} \equiv G_{WPN} + i\Omega C_{WPN} \tag{23}$$

where

$$G_{WPN} \equiv \Omega^{\frac{1}{2}}/2A \tag{24}$$

and

$$C_{WPN} \equiv (2A\Omega^{\frac{1}{2}})^{-1} \tag{25}$$

Now when C_{iN} is replaced by C_{WSN} and R_{iN} by R_{WSN} in eqns. (16) and (17) one obtains

$$C_{PN} \cong 1 + \frac{(A\Omega^{\frac{1}{2}})^{-1}}{1+[1+\Omega^{\frac{1}{2}}(R_{EN}/A)]^2} \tag{26}$$

and

$$G_{PN} \cong G_{DN} + \frac{(\Omega^{\frac{1}{2}}/A)[1+\Omega^{\frac{1}{2}}(R_{EN}/A)]}{1+[1+\Omega^{\frac{1}{2}}(R_{EN}/A)]^2} \tag{27}$$

Since $(\Omega^{\frac{1}{2}} R_{EN}/A) = R_{EN}/R_{WSN} \cong R_{EN}/R_{iN}$ here, we need to consider the two cases: (A) $(R_{EN}/R_{iN}) \ll 1$, and (B) $(R_{EN}/R_{iN}) \gg 1$.

In case (A) we have

$$C_{PN} \cong 1+(A\Omega^{\frac{1}{2}})^{-1}/2 \equiv 1 + C_{WPN} \cong 1+(C_{iN}/2) \tag{28}$$

and

$$G_{PN} \cong G_{DN} + (\Omega^{\frac{1}{2}}/A)/2 = G_{DN} + G_{WPN} \tag{29}$$

These equations lead to the important slope ± 0.5 regions of Figs. 15a and 15b which there occur for $\pi_m \lesssim 10^{-4}$, the value of M^{-1}.

Low-frequency saturation is approached when $\Omega \lesssim 10\ \pi_m M^{-2}$, and C_{PN} approaches the plateau value $C_{PSN} = 1 + C_{iSN} \cong M\delta_p^{\frac{1}{2}}$ when $\Omega \gtrsim \pi_m$. Figure 15b shows that this $r_p = r_n = 0$, $\pi_m < M^{-1}$ plateau is also reached for $\pi_m < M^{-1}$ even in the $r_p = 0$, $r_n = \infty$ discharge situation. As pointed out earlier, this plateau is reached when the mobility of the discharging carrier (here μ_n) is sufficiently low and the frequency sufficiently high that the discharging carrier has insufficient time to discharge and is essentially immobile; it then acts as though it were completely blocked. If we take the necessary condition as $\Omega \gtrsim 10\pi_m$, then the actual radial frequency corresponding to the choice of the equality sign is

$$\begin{aligned} \omega = \omega_b &\equiv 10\ \mu_n/\mu_p C_g R_\infty \\ &= (4\pi e/\varepsilon)(10\ z_p p_i \mu_n)(1+\pi_m) \\ &\cong 40\ \pi e z_p p_i \mu_n/\varepsilon \end{aligned} \tag{30}$$

where the last equation follows on using $\pi_m \ll 1$. As before, the plateau region gives way to a simple Debye dispersion region proportional to Ω^{-2} when $\Omega > (M\delta_p^{\frac{1}{2}})^{-1}$.

The various regions which appear when $\pi_m \ll 1$ and especially when $\pi_m M \ll 1$ as well are described for C_{PN} and C_{iN} in Table 2. Although the Ω-values chosen to divide the various regions are somewhat approximate, they are quite adequate for usual situations. In the $(r_p,\ r_n;\ \pi_m,\ \pi_z;\ 0,\ M)$ situation with $0 \leqslant \pi_m \ll 1$ the

TABLE 2

RESPONSE REGIONS FOR C_{PN} AND C_{iN} WHEN $\pi_m \ll 1$

Region	*A*	*B*	*C*	*D*	*E*
Description:	Low-frequency-limiting saturation	Approximate Z_{TN}, Y_{TN} Warburg response	Double-layer plateau	External transition	Dielectric relaxation
C_{PN} (Case A)	C_{PN0}	$C_{PN0} > C_{PN} \simeq C_{WPN} > C_{PSN}$	C_{PSN}	$< C_{PSN}$	C_g
C_{iN}	C_{iN0}	$C_{iN0} > C_{iN} \simeq C_{WSN} > C_{iSN}$	C_{iSN}		$< C_{iSN}$
Ω range	$0 \leqslant \Omega \lesssim 10\,\pi_m M^{-2}$	$40\,\pi_m M^{-2} \lesssim \Omega < \pi_m$	$10\,\pi_m \leqslant \Omega \lesssim (10\,M\delta_p^{\ddagger})^{-1}$ $10\,\pi_m \leqslant \Omega \lesssim 0.1$	$(M\delta_p^{\ddagger})^{-1} < \Omega \lesssim 0.1$	$0.1 \lesssim \Omega < \infty$
Ω division points	$10\,\pi_m M^{-2}$	π_m	$(M\delta_p^{\ddagger})^{-1}$	0.1	

appropriate expression for C_{iSN} is $g_p^{-2}[M\delta_p^{\frac{1}{2}}-1]$; $G_{EN}\cong[1+(r_p/2)]^{-1}+\pi_m[1+(r_n/2)]^{-1}$; and $G_{DN}\cong[1+(2/r_p)]^{-1}+\pi_m[1+(2/r_n)]^{-1}$. Thus, when $r_p=0$. $R_{DN}=\pi_m^{-1}[1+(2/r_n)]$ and may be neglected for sufficiently small π_m. In addition, R_{iN} will be appreciably less than unity in the plateau region and may be neglected compared to $R_{EN}\cong 1$. When $r_p=0$ Fig. 17 then shows the approximate equivalent circuit of the overall system. Of course when $\pi_m \ll r_p \ll \pi_m^{-1}$, the R_∞ in Fig. 17 must be replaced by $R_E\cong[1+(r_p/2)]R_\infty$ and the resistance $R_D\cong[1+(2/r_p)]R_\infty$ must be connected in parallel with C_g.

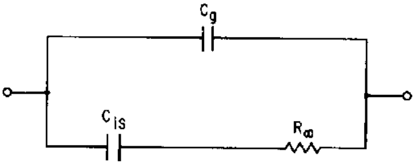

Fig. 17. Approximate equivalent circuit in the plateau region (Regions C and D of Table 2).

In order to find under what conditions (R_{EN}/R_{iN}) is smaller or greater than unity, we require an expression for the normalized Warburg parameter A. In the approximate Warburg region, the exact expression for Z_{iN} given earlier[4] may be simplified under the overlapping conditions $M \gg 1$, $10 \lesssim M^2 b\Omega$, $(a-1)\Omega \ll 1$, $\Omega[b(a-1)]^{\frac{1}{2}} \ll 1, (b\Omega)^{\frac{1}{2}} \ll \delta_n\delta_p[(g_p-g_n)/g_z]^2$, and $b\Omega \ll \delta_n\delta_p(g_p-g_n)^2/g_s M$. Note that for $r_p=0$, $r_n=\infty$ the last two conditions reduce to $(b\Omega)^{\frac{1}{2}} \ll \delta_n/\delta_p \equiv \pi_z$, and $b\Omega \ll \infty$. The condition $10 \lesssim M^2 b\Omega$ leads to $\Omega \gtrsim 10\,M^{-2}(2+\pi_z+\pi_z^{-1})/(2+\pi_m+\pi_m^{-1})$ when the exact relations $(\varepsilon_n\varepsilon_p)^{-1}\equiv(2+\pi_m+\pi_m^{-1})$ and $(\delta_n\delta_p)^{-1}\equiv(2+\pi_z+\pi_z^{-1})$ are used. For $\pi_z=1$, this reduces to $\Omega \gtrsim 40\ M^{-2}\pi_m$, $10\ M^{-2}$, and $40\ (M^2\pi_m)^{-1}$ for $\pi_m \ll 1$, $\pi_m=1$, and $\pi_m \gg 1$, respectively. When $M^2 b\Omega < 10$, one approaches the low-frequency saturation region.

The result of the Z_{iN} simplification yields $Z_{iN}\cong Z_{WN}$ together with the following expression for A,

$$A \equiv [MG_{pn}(2\varepsilon_n\varepsilon_p\delta_n\delta_p)^{\frac{1}{2}}]^{-1} \tag{31}$$

applying for $(r_p, r_n; \pi_m, \pi_z; 0, M)$. Here

$$G_{pn} \equiv [(g_p-g_n)/g_p g_n]^2 \tag{32}$$

The symmetric function G_{pn} is unity for $r_p=0$, $r_n=\infty$ and, in the $r_p=0$, $r_n<\infty$ case, decreases only slowly as r_n decreases. For example for $r_n=200$, $G_{pn}\cong 0.99$. Since G_{pn} is symmetric in n and p, so also is A.

Now since $(R_{EN}/R_{iN})\cong\Omega^{\frac{1}{2}}/AG_{EN}$ in the Warburg region, we find

$$R_{EN}/R_{iN} \cong M\Omega^{\frac{1}{2}}G_{pn}(g_p g_n/g_s)[2\varepsilon_n\varepsilon_p\delta_n\delta_p]^{\frac{1}{2}} \tag{33}$$

Now for $r_p=0$, $r_n=\infty$, this result reduces to

$$\begin{aligned} R_{EN}/R_{iN} &\cong M\Omega^{\frac{1}{2}}[2\varepsilon_n\delta_n\delta_p/\varepsilon_p]^{\frac{1}{2}} \\ &= M[\pi_m\Omega]^{\frac{1}{2}}[2\delta_n\delta_p]^{\frac{1}{2}} \\ &= M[\pi_m\Omega]^{\frac{1}{2}}/[1+0.5(\pi_z+\pi_z^{-1})]^{\frac{1}{2}} \end{aligned} \tag{34}$$

Again since the range of π_z is limited, the π_z terms in the last expression may be neglected for most purposes. At the large-Ω edge of the Warburg region where $\Omega=\pi_m$ when $\pi_m \ll 1$, $(R_{EN}/R_{iN}) \sim M\pi_m$. Thus, in order for case (A) to hold in Region B of Table 2 we must have $\Omega \ll (M^2\pi_m)^{-1}$ and $M\pi_m \ll 1$. It is, of course, essentially just the $M\pi_m \ll 1$ condition that ensures that Region C, the plateau of Table 2, is appreciable. When $M\pi_m \cong 1$, Fig. 15b shows no plateau.

Before considering case (B), let us first examine the intermediate $(0, \infty; 1, 1; 0, M)$ situation. Here $(R_{EN}/R_{iN}) = M(\Omega/2)^{\frac{1}{2}}$ and low-frequency saturation occurs near $\Omega = 10\,M^{-2}$. Thus the $(R_{EN}/R_{iN}) = 1$ condition is almost within Region A of Table 2. In this region, of course $Z_{iN} \neq Z_{WN}$, however. Figures 15b and 16a show that for $Z_{iN} \cong Z_{WN}$ in the present situation, we must have $\Omega \gtrsim 32M^{-2}$. At this point $(R_{EN}/R_{iN}) = 4$. The denominator of eqns. (25) and (26) is then 26, sufficiently large that explicit external Warburg behavior, as in Region B of Table 2, does not appear. We will thus next consider the limiting $(R_{EN}/R_{iN}) \gg 1$ situation. Now consider case (B), where eqn. (34) yields $\Omega \gg (M^2\pi_m)^{-1}$, consistent with the general simplification condition $\Omega \gtrsim 10(bM^2)^{-1}$, which itself allows case (B) behavior even for π_m as small as 10^{-2} when $\Omega \gtrsim 10^{-4}$ in the present $M=10^4$ case. Now eqns. (26) and (27) lead to

$$C_{PN} \cong 1+(\Omega^{\frac{3}{2}} R_{EN}^2/A)^{-1} \tag{35}$$

and

$$G_{PN} \cong G_{DN} + G_{EN} = 1 \tag{36}$$

On using the earlier expression for A, eqn. (35) becomes, for $(r_p, r_n; \pi_m, \pi_z; 0, M)$,

$$C_{PN} \cong 1+[\Omega^{\frac{1}{2}} M \{(g_p - g_n)/g_s\}^2 (2\varepsilon_n\varepsilon_p\delta_n\delta_p)^{\frac{1}{2}}]^{-1} \tag{37}$$

As mentioned earlier, equations such as (37) also hold in the extrinsic conduction situation when the ε's and δ's are suitably redefined[4]. When $r_p=0$ and $r_n=\infty$, eqn. (37) reduces to

$$C_{PN} \cong 1+[(\varepsilon_p\Omega^{-1})^{\frac{1}{2}}\varepsilon_n^{-\frac{1}{2}}/M(2\delta_n\delta_p)^{\frac{1}{2}}] \tag{38}$$

and for $\pi_z=1$ as well to

$$C_{PN} \cong 1+[2^{\frac{1}{2}}\Omega^{-\frac{1}{2}}\varepsilon_p^{\frac{3}{2}}\varepsilon_n^{-\frac{1}{2}}M^{-1}] \tag{39}$$

This result describes those curves of Fig. 15b which show a slope of -1.5. In the $\pi_z=\pi_m=1$ case,

$$C_{PN} \cong 1+(2^{\frac{1}{2}} M\Omega^{\frac{3}{2}})^{-1} \tag{40}$$

To illustrate the size of the second term in (38), take $(R_{EN}/R_{iN}) = 10$ and use this value in (34) and the result in (38). At this point, where $\Omega = 100\ \varepsilon_p/2\varepsilon_n\delta_n\delta_p M^2$,

$$C_{PN} \cong 1+2\varepsilon_n\delta_n\delta_p 10^{-3} M^2 \tag{41}$$

For $\pi_z=1$ and $\pi_m \gg 1$, this equation yields $C_{PN} \cong 1+(M^2/2000)$, which can still be considerably larger than the plateau value, $M\delta_p^{\frac{1}{2}}$, for large M.

In case (B), where Warburg behavior of Z_{iN} requires $\Omega \gtrsim 40(M^2\pi_m)^{-1}$, and C_{iN} approaches low-frequency saturation for $\Omega \lesssim 10(M^2\pi_m)^{-1}$ when $\pi_m \gg 1$, the curves of Fig. 15b show that $C_{PN} \to C_{PN0}$ in this case when $\Omega < 10(M^2\pi_m)^{-1}$. The initial decrease of C_{PN} below C_{PN0} thus arises here both from the decrease of C_{iN} and from an increase in the denominator of (26).

When the expression for A of eqn. (31) is converted to one for A_0 through using eqn. (7), one obtains in the present two-electrode situation

$$A_0 = [(e^2/2^{\frac{1}{2}}kT)(G_{pn}/2)(z_n n_i + z_p p_i) \times [\{(z_p D_p)^{-1} + (z_n D_n)^{-1}\}\{z_p^{-1} + z_n^{-1}\}]^{-\frac{1}{2}}]^{-1} \quad (42)$$

where mobilities have been converted to diffusion coefficients through the relation $D_i = (kT/ez_i)\mu_i$. This result for A_0 will be considered in more detail in the next section and compared to earlier expressions for the Warburg parameter. It simplifies for $(0, \infty; \pi_m, 1; 0, M)$ and $z_p = z_n \equiv z_e$ to

$$A_0 = [(z_e^2 e^2 c_i/2kT)\{D_p^{-1} + D_n^{-1}\}^{-\frac{1}{2}}]^{-1} \quad (43)$$

where $n_i = p_i \equiv c_i$ has been used, a condition following from $\pi_z = 1$. Since A_0 is independent of l and thus intensive, Z_W is also intensive as it should be.

The unnormalized form of eqn. (28), applying in the case (A) Warburg region, is just

$$C_P \cong C_g + (2\omega^{\frac{1}{2}} A_0)^{-1} \quad (44)$$

Similarly, the case (**B**) result given in eqn. (35) becomes

$$C_P \cong C_g + (A_0/R_E^2 \omega^{\frac{3}{2}}) \quad (45)$$

In the $z_p = z_n = 1$, $(0, \infty; \pi_m, 1; 0, M)$ case, this result reduces to

$$\begin{aligned} C_P &\cong C_g + (A_0 \varepsilon_p^2/R_\infty^2 \omega^{\frac{3}{2}}) \\ &= C_g + (2ec_i/l^2)[\mu_p(D_p/D_n)^{\frac{1}{2}}(D_p + D_n)^{\frac{1}{2}}]\omega^{-\frac{3}{2}} \end{aligned} \quad (46)$$

Although the Warburg $(C_P - C_g)$ of eqn. (44) is intensive, the $(C_P - C_g)$ of eqn. (46) is certainly not.

For this same $r_p = 0$, $r_n = \infty$ situation, Friauf[23] obtained the expression (rewritten in the present notation)

$$C_P = (2ec_i/l^2)[\mu_n(D_n/D_p)^{\frac{1}{2}}(D_n + D_p)^{\frac{1}{2}}]\omega^{-\frac{3}{2}} \quad (47)$$

Except for the absence of C_g and the subscript transformation n→p and p→n, the results are the same. In addition, however, Friauf gives no range of ω defining the region of applicability of this result. The n–p transformation is just that here changes $(0, \infty; \pi_m, 1; 0, M)$ to $(\infty, 0; \pi_m, 1; 0, M)$ or its equivalent, $(0, \infty; \pi_m^{-1}, 1; 0, M)$. Thus Friauf's result applies not, as he states, for $(0, \infty)$ but for $(\infty, 0)$ boundary conditions. When π_m is appreciably different from unity, Friauf's result, when incorrectly applied to the $(0, \infty)$ case, leads to C_P values which will differ very significantly from the correct values since the ratio of his result to the correct one is, on neglecting C_g, just π_m^2.

Figure 15b shows that $\Omega \lesssim 10^{-3}$ is necessary for very much case (**B**) behavior to appear. Therefore, for case (**B**) we may write $(\pi_m M^2)^{-1} \ll \Omega \lesssim 10^{-3}$. Thus here $\pi_m M^2 \gg 1$, as compared to the $M\pi_m \lesssim 1$ condition required for case (A).

We have devoted especial attention to the curves of Fig. 15b because most experimental results yield similar sorts of curves. Figures 18 and 19 show how the $\pi_m = \pi_z = 1$ curves of Fig. 15 change when r_p or r_n are separately varied. The Tables in these Figures also indicate how R_{iN0}, R_{EN}, and R_{DN} vary. Nore from

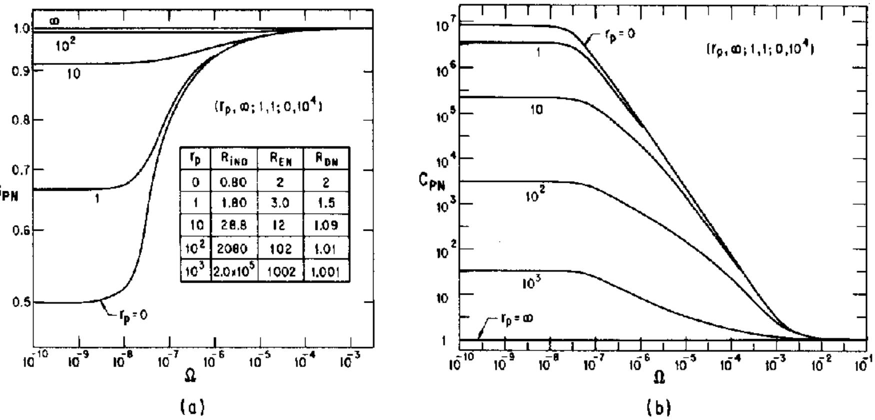

Fig. 18. Normalized frequency response of G_{PN} and C_{PN} for the (r_p, ∞; 1, 1; 0, 10^4) situation.

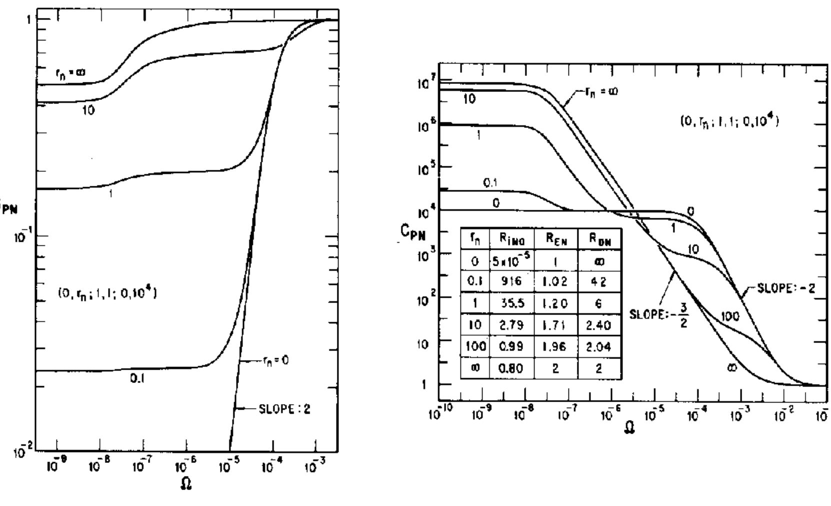

Fig. 19. Normalized frequency response of G_{PN} and C_{PN} for the (0, r_n; 1, 1; 0, 10^4) situation.

Fig. 18b that for small r_p there is still an appreciable region of approximately -1.5 slope present and that regions with negative slopes nearer zero appear as r_p increases. On the other hand, Fig. 19 shows that a new dispersion region appears when $r_p = 0$ and $r_n < \infty$. This result is consistent, of course, with the three arcs which appear in Fig. 5b for the same (0, r_n; 1, 1; 0, 10^4) situation.

Some comparison of theoretical and experimental Warburg region behavior will be presented in the next Section from an electrochemical point of view. But a great deal of experimental evidence is available for solids and fused salts where C_P or the apparent dielectric constant, ε_a, shows ω^{-m} dependence over appreciable ranges with $0 \leqslant m \leqslant 2$ and especial concentrations of values around 0.5 and 1.5. Reference has already been given to the work of Friauf[23] ($m \sim 1.5$) and the author[11] ($m = 1.5$, 2). In addtion some of the earlier literature has been summarized elsewhere[1–4]. Here only a few relatively recent experimental results will be briefly mentioned.

Some of the types of frequency response results with which we shall be concerned have been ascribed to the presence of a continuous or discrete distribution of relaxation times. While this explanation will be appropriate in some cases, a partially blocking space-charge theory[2,4,23] explanation seems more likely in most cases, especially those where very high values of C_p or ε_a appear at low frequencies.

Michel *et al.*[24] have seen ω^{-m} behavior in diverse solid materials with $0<m<1.5$ and numerous results with $m\sim 1$. Cochrane and Fletcher[25] have found ε_a *versus* frequency curves rather similar to some of those of Figs. 15b and 19b for single crystal AgI. Armstrong and Race[26] have observed good $r_p=r_n\cong 0$ type curves in liquid electrochemical situations. Allnatt and Sime[27], working with single crystal NaCl, found many slopes in the range $1.3<m\leqslant 1.9$. In contrast, Lancaster[28] found many slopes of ~ 1.5 or less for thin films of cerous fluoride.

Some application of the results of the present theory to the experimental measurements of Mitoff and Charles[29] has already been given[21,30]. Although these authors question the applicability of some of the conclusions[31], their reasons do not seem convincing[21]. Mitoff and Charles found m-values of 0.5, 1, 1.5, and 2 for a variety of solid materials. Also, Tibensky and Wintle[32] found series capacitance frequency dependences with $m\cong 0.5$ for KBr single crystals, although the conversion from measured parallel capacitance to calculated series capacitance was not carried out using one of the circuits of Fig. 1. Nevertheless, Warburg response appears and may be associated with a $\pi_m\ll 1$ situation. Finally, Maeno[33], working with pure and doped single crystals of ice, has found many ε_a curves with shapes like those of Figs. 15b and 19b. Both $m\sim 0.5$ and $m\sim 1.5$ values appear. He also gives impedance-plane results consistent with those of Fig. 3b. Although the data indicate the high probability of an incompletely blocking space-charge situation, Maeno suggests a distribution of relaxation times explanation.

Incidentally, for simplicity I have presented no discussion of the many different doping and electrode situations applicable for the various experiments mentioned above. Both essentially blocking and non-blocking (*e.g.*, $r_p\sim 0$, $r_n\sim\infty$) electrodes were used. Not all the materials measured were in an intrinsic conduction temperature region but many were. It is hoped to compare intrinsic–extrinsic conduction theoretical predictions[4] and appropriate experimental results, with especial emphasis on temperature dependence, in a later paper[5].

VI. DETAILED CONSIDERATION OF APPROXIMATE WARBURG RESPONSE

A. Analysis

In this Section, we shall be particularly concerned with the region showing approximate Warburg response of Z_{iN}. As we have seen, strong *external* Warburg response only appears for $\pi_m\lesssim M^{-1}$ and leads to Region B of Table 2. But Fig. 16 shows that approximate Warburg response appears in Z_{iN} in certain frequency regions for all π_m. Thus, to the degree that experimental accuracy allows Z_i to be obtained adequately from Z_T, Warburg response can be derived from even the $m=1.5$ regions of case (B) of the last Section, where π_m may appreciably exceed unity.

As an extreme example, consider the $(0, \infty; 999, 1; 0, 10^4)$ curve of Fig. 15b at $\Omega = 10^{-9}$, where the overall dissipation factor, $D_T \equiv G_{PN}/\Omega C_{PN} \equiv -\mathrm{Re}(Z_{TN})/\mathrm{Im}(Z_{TN})$, is about 7085. Now although Seitz *et al.*[34] have described a technique which allows measurement of C_P and G_P with reasonable accuracy up to D_T values of about 10^4, the main difficulty arises here in the calculation of C_i and R_i from C_P and G_P measurements. Assume that C_g and R_∞ can be obtained from $\Omega \gtrsim 0.1$ measurements and G_D from measurements in the low-frequency saturation region, $\Omega \lesssim b^{-1}M^{-2}$. Then at a given ω value of interest, Ω, C_{PN}, G_{PN}, G_{DN}, and G_{EN} may be calculated. The solution of eqns. (16) and (17) for C_{iN} and R_{iN} yields

$$C_{iN} = (C_{PN} - 1) + [(G_{PN} - G_{DN})^2/\Omega^2(C_{PN} - 1)] \tag{48}$$

and

$$R_{iN} = [(G_{PN} - G_{DN})/\{\Omega^2(C_{PN} - 1)^2 + (G_{PN} - G_{DN})^2\}] - R_{EN} \tag{49}$$

For the (0, ∞; 999, 1; 0, 10^4) situation, the terms involving $(G_{PN} - G_{DN})$ dominate. But here $G_{PN} \cong G_{DN} \cong 1$, and $(G_{PN} - G_{DN}) \cong 8.59 \times 10^{-4}$. The problem is thus evident: G_{PN} and G_{DN} must be known to one part in 10^4 or better to achieve even moderate accuracy in C_{iN} and R_{iN}. Of course when π_m is appreciably smaller, this problem is much less severe.

Some comparison has already been given[35] of the present expression for the Warburg parameter A_0, which applies for a binary system without a supporting indifferent electrolyte, with the conventional expression. In the usual derivation[36,37] of A_0, electroneutrality is assumed everywhere, implicitly or explicitly arising from the presence of a supporting electrolyte whose ions are taken to be completely blocked. Then the contributions to A_0 are, for example, from the diffusion of oxidizing and reducing species in the neighborhood of the working electrode. The situation is considerably different in the present work. Here in the $r_p = 0$, $r_n = \infty$ case, for example, charges are coupled through Poisson's equation; charge of one sign is completely blocked; and only that of opposite sign reacts at the electrode. Further, we have considered the situation of two identical electrodes. Thus, in the simplest case the charged state of the reacting species is created by charge transfer at one electrode and destroyed at the other. These processes are reversed when the polarities of the electrodes reverse.

It is believed that the physical situation described above and analyzed earlier[2,4] is a plausible one for the unsupported binary electrolyte and for the two carrier intrinsic conduction situation in solids. Some modification is necessary to pass from the present assumption of two identical, plane-parallel electrodes, usual for experiments with solids, to that of a small working electrode and a large indifferent counter electrode, common for work with liquid electrolytes. To good approximation, it seems plausible to pass from two identical electrodes each of area σ to a single working electrode of area σ by dividing intensive impedance components, associated with processes at the electrodes, by two. Thus, in the present situation, where only specific quantities are considered, ${}^{(1)}Z_W \cong 0.5\,{}^{(2)}Z_W$, where the superscripts indicate one or two electrodes. It follows that ${}^{(1)}A_0 \cong 0.5\,{}^{(2)}A_0$. Non-intensive quantities such as C_g and R_∞ cannot be treated in this way, of course. For the actual single working electrode situation used in an experiment, C_g and R_∞ should either be calculated accurately or, preferably, directly measured in the region where they dominate, $\Omega > 0.1$.

The above prescriptions may be adequate when $Z_T - R_\infty \cong Z_W$ to good approximation, but they are impractical to apply accurately in the present binary case where Z_T and Z_i may be made up of both intensive and extensive circuit elements mixed together in complicated fashion. In a recent preliminary note[35], comparison of A_0's was made for a single working electrode situation. Here such comparison will be made for two identical electrodes by using ${}^{(2)}A_0 = 2\,{}^{(1)}A_0$, where ${}^{(1)}A_0$ is the conventional result. We may then continue to deal directly with the unmodified two-electrode theoretical circuit elements C_g, R_E, R_D, and Z_i.

The conventional supported result for oxidizing and reducing species with concentration c_O and c_R, diffusion coefficients D_O and D_R, and stoichiometric factors ν_O and ν_R may be written in the two-electrode case as[36,37]

$$A_0 = [(n^2 e^2/2^{\frac{1}{2}} kT)\{(\nu_O^2/c_O D_O^{\frac{1}{2}}) + (\nu_R^2/c_R D_R^{\frac{1}{2}})\}^{-1}]^{-1} \tag{50}$$

where n is here the number of electrons participating in the reaction. This result may be compared to that of eqn. (42) for z_p and z_n arbitrary in the $(r_p, r_n; \pi_m, \pi_z; 0, M)$ situation. The explicit result for $(0, \infty; \pi_m, 1; 0, M)$ and $z_p = z_n \equiv z_e$ has already been given in eqn. (43).

Although eqns. (43) and (50) are still notably different in ways readily amenable to experimental verification, in the special situation where $z_e^2 = (n/\nu_O)^2 = (n/\nu_R)^2$, $D_O = D_R = D_n = D_p$, and $c_O = c_R = c_i$, the equations yield the same result. It is this result which is, in fact, most often used to analyze experimental measurements, probably because of lack of separate information on D_O, D_R, etc. Although the n_i, p_i, and c_i quantities in the present treatment are equilibrium bulk values, as are c_O and c_R, the diffusion coefficients D_n and D_p refer to charged species in the present binary case while the question of the charge states of the possibly many species considered in the conventional supported case[36] does not enter the derivation explicitly except through the presence of n. Comparison between the present result for A_0 and a more pertinent generalization of the conventional result will be carried out later in this Section.

Let us now consider a somewhat better approximation for Z_i than the Z_W employed in the last Section. Let $c \equiv (\delta_n/\varepsilon_n) - (\delta_p/\varepsilon_p)$. Next apply the inequalities $M \gg 1$, $\Omega \geqslant (10/bM^2)$, $\Omega(a-1) \ll 1$, $\Omega|c| \ll 1$, and $\Omega|c| \ll |(g_p - g_n)/g_n|$ to simplify the complete expression for Z_{iN} given earlier[4]. The result of very considerable manipulation can be written as

$$Y_{iN} \cong G_{WPN}\left[\frac{(1-\delta_1-\delta_2)+\mathrm{i}(1+\delta_2+\delta_3)}{(1+\alpha_1)+\mathrm{i}\alpha_2}\right] \tag{51}$$

where

$$\delta_1 \equiv (2/b\Omega M^2)^{\frac{1}{2}} \tag{52}$$

$$\begin{aligned}\delta_2 &\equiv \Omega(r-1)G_{EN}^2 G_{pn}^{-1}/g_s \varepsilon_p \varepsilon_n \\ &\cong \Omega(M/g_s)G_{EN}^2 G_{pn}^{-1}(2+\pi_m+\pi_m^{-1})\end{aligned} \tag{53}$$

$$\begin{aligned}\delta_3 &\equiv (r-1)(2\Omega/\varepsilon_n\varepsilon_p\delta_n\delta_p)^{\frac{1}{2}} M^{-1} H_{pn} \\ &\cong (2\Omega)^{\frac{1}{2}} H_{pn}[(2+\pi_m+\pi_m^{-1})(2+\pi_z+\pi_z^{-1})]^{\frac{1}{2}}\end{aligned} \tag{54}$$

$$\alpha_1 \equiv g_s^{-1}(\delta_1^{-1}-1) \tag{55}$$

and

$$\alpha_2 \equiv g_s^{-1}[\delta_1^{-1} + \Omega(a-1)(r-1)] \tag{56}$$

Here,

$$H_{pn} \equiv [(g_z^2 - g_s)/(g_p - g_n)^2] \tag{57}$$

When g_p or g_n is infinite, H_{pn} reduces to δ_n^2 or δ_p^2, respectively. For $r_p = 0$, $r_n \gg 1$, $\pi_m \lesssim 1$, and $\pi_z = 1$, $H_{pn} \cong 0.25$.

Although eqn. (51) is only an approximate result for the Warburg region, it nevertheless maintains the original symmetry of Z_{iN} which ensures that Z_{iN} is the same for $(r_p, r_n; \pi_m, \pi_z; 0, M)$ and for $(r_n, r_p; \pi_m^{-1}, \pi_z^{-1}; 0, M)$. Note that when g_p or g_n is infinite, δ_2, α_1, and α_2 are all zero. Since we require $\Omega \geqslant (10/bM^2)$ here, eqn. (52) yields the result $\delta_1 \leqslant 5^{-\frac{1}{2}} \cong 0.447$. It will be considerably smaller away from the low-Ω edge of the Warburg region.

Let us now introduce some new quantities and write

$$\begin{aligned} Y_{iN} &\equiv G_{KN} + i\Omega C_{KN} \\ &\equiv Y_{WN} + Y_{\theta N} \end{aligned} \tag{58}$$

$$Y_{\theta N} \equiv G_{\theta PN} + i\Omega C_{\theta PN} \tag{59}$$

and

$$\begin{aligned} Z_{iN} &\equiv R_{iN} + (i\Omega C_{iN})^{-1} \\ &\equiv Z_{WN} + Z_{\theta N} \end{aligned} \tag{60}$$

$$Z_{\theta N} \equiv R_{\theta SN} + (i\Omega C_{\theta SN})^{-1} \tag{61}$$

We have $Z_{iN} \equiv Y_{iN}^{-1}$ here but have not assumed $Z_{\theta N} \equiv Y_{\theta N}^{-1}$. The above exact relations lead to

$$G_{KN} \equiv G_{WPN} + G_{\theta PN} \tag{62}$$

$$C_{KN} \equiv C_{WPN} + C_{\theta PN} \tag{63}$$

$$R_{iN} \equiv R_{WSN} + R_{\theta SN} \tag{64}$$

and

$$C_{iN}^{-1} \equiv C_{WSN}^{-1} + C_{\theta SN}^{-1} \tag{65}$$

Although eqns. (62) through (65) are always possible when the θ quantities are arbitrary, we shall be particularly interested here in relatively small deviations from Warburg behavior, where the second term in each equation is substantially smaller in magnitude than the first term. Further, we shall also be interested in any frequency region where the second terms are substantially independent of frequency. In this region, let us denote the constant parts of the second terms with a subscript "C". Thus for example, over a certain Ω range $G_{\theta PN} \cong G_{CPN}$, a frequency-independent circuit parameter. Equivalent circuits involving the above θ-subscript quantities will be considered in the next part of this Section. Note that eqn. (64) suggests that $R_{\theta S}$ (or R_{CS}) plays a role in the present unsupported case equivalent to the equilibrium charge transfer resistance R_θ appearing in the usual supported situation. A detailed comparison will be made later in this Section.

Let us now assume $\alpha_1 \ll 1$ and $\alpha_2 \ll 1$ in eqn. (51). On series inverting the denominator, retaining only first-order terms, and ignoring all small frequency-dependent product terms, one is immediately led to

$$G_{\theta \mathrm{PN}} \cong -G_{\mathrm{WPN}}[(\delta_1+\delta_2)+(\alpha_1-\alpha_2)] \tag{66}$$

and

$$C_{\theta \mathrm{PN}} \cong C_{\mathrm{WPN}}[(\delta_2+\delta_3)-(\alpha_1+\alpha_2+\alpha_3)] \tag{67}$$

where

$$\alpha_3 \equiv C_{\mathrm{WPN}}^{-1} H_{\mathrm{pn}} G_{\mathrm{pn}}(M/g_s) \tag{68}$$

The frequency-independent parts of the above expressions are, on ignoring the difference between $(r-1)$ and M,

$$G_{\mathrm{CPN}} \equiv -G_{\mathrm{WPN}}\delta_1 = -\varepsilon_{\mathrm{p}}\varepsilon_{\mathrm{n}} G_{\mathrm{pn}} = -G_{\mathrm{pn}}/(2+\pi_{\mathrm{m}}+\pi_{\mathrm{m}}^{-1}) \tag{69}$$

and

$$\begin{aligned} C_{\mathrm{CPN}} &\equiv C_{\mathrm{WPN}}[\delta_3 - 2(g_s\delta_1)^{-1} - \alpha_3] \\ &\cong MG_{\mathrm{pn}}[H_{\mathrm{pn}} - \delta_{\mathrm{n}}\delta_{\mathrm{p}}(M/g_s)] \end{aligned} \tag{70}$$

Because of the presence in $G_{\theta \mathrm{PN}}$ and $C_{\theta \mathrm{PN}}$ of somewhat compensating terms involving Ω^m and Ω^{-m}, where $m \neq 0$, the approximations $G_{\theta \mathrm{PN}} \simeq G_{\mathrm{CPN}}$ and $C_{\theta \mathrm{PN}} \simeq C_{\mathrm{CPN}}$ hold good over an appreciable Ω range.

If we next write an expression for Z_{iN} from (51), now assume δ_1, δ_2, and δ_3 all small compared to unity, invert the denominator of Z_{iN}, and again neglect all small frequency-dependent products, we obtain

$$R_{\theta \mathrm{SN}} \cong R_{\mathrm{WSN}}[\alpha_1+\alpha_2(1+\delta_1)-\delta_2-(\delta_3+2\delta_1\delta_2)(1-g_s^{-1})] \tag{71}$$

and

$$C_{\theta \mathrm{SN}}^{-1} \cong C_{\mathrm{WSN}}^{-1}[\alpha_1(1+\delta_1)-\alpha_2+(\delta_1+\delta_2)] \tag{72}$$

The corresponding frequency-independent quantities are

$$\begin{aligned} R_{\mathrm{CSN}} &\equiv R_{\mathrm{WSN}}[2(g_s\delta_1)^{-1}-(\delta_3+2\delta_1\delta_2)(1-g_s^{-1})+g_s^{-1}\delta_1\Omega(a-1)(r-1)] \\ &= (g_s G_{\mathrm{pn}}\varepsilon_{\mathrm{n}}\varepsilon_{\mathrm{p}})^{-1} - \left(\frac{r-1}{M^2}\right)\left(\frac{G_{\mathrm{pn}}^{-1}}{\delta_{\mathrm{n}}\delta_{\mathrm{p}}}\right) \\ &\qquad \times \left[(\varepsilon_{\mathrm{n}}\varepsilon_{\mathrm{p}})^{-1}\left\{H_{\mathrm{pn}}(1-g_s^{-1}) + \left(\frac{2G_{\mathrm{EN}}^2}{G_{\mathrm{pn}}g_s}\right)\right\} + \left(\frac{1-a}{g_s}\right)\right] \\ &\cong (G_{\mathrm{pn}}\varepsilon_{\mathrm{n}}\varepsilon_{\mathrm{p}})^{-1}[g_s^{-1}-(H_{\mathrm{pn}}/M\delta_{\mathrm{n}}\delta_{\mathrm{p}})] \end{aligned} \tag{73}$$

and

$$\begin{aligned} C_{\mathrm{CSN}} &\equiv C_{\mathrm{WSN}}[\delta_1(1-g_s^{-1})]^{-1} \\ &\cong (\delta_{\mathrm{n}}\delta_{\mathrm{p}}M^2)G_{\mathrm{pn}} \end{aligned} \tag{74}$$

where g_s^{-1} has been neglected compared to terms of order unity in the last forms of eqn. (70) and in eqns. (73) and (74). These simplified results will be used as the definitions of the constant quantities from here on. Note that the larger of the two contributions to C_{iN0} when r_{p} and r_{n} are appreciably different is just $(\delta_{\mathrm{n}}\delta_{\mathrm{p}}M^2G_{\mathrm{pn}}/3)$; thus, C_{CSN} as given above is then appreciably larger than C_{iN0}. Table 3 shows how the various frequency-independent elements depend on several quantities of interest for $(0, r_{\mathrm{n}};\, \pi_{\mathrm{m}}, \pi_z;\, 0, M)$ with $\pi_{\mathrm{m}} \ll 1$.

Using the properties of the Warburg impedance, one may readily derive the exact equation

$$Y_{\mathrm{WN}}Z_{\theta \mathrm{N}} + Y_{\theta \mathrm{N}}Z_{\mathrm{WN}} + Z_{\theta \mathrm{N}}Y_{\theta \mathrm{N}} = 0 \tag{75}$$

TABLE 3

DEPENDENCE OF NORMALIZED, FREQUENCY-INDEPENDENT CIRCUIT ELEMENTS ON VARIOUS QUANTITIES FOR $(0, r_n; \pi_m, \pi_z; 0, M)$, WITH $\pi_m \ll 1$, AND SEVERAL (M/r_n) SITUATIONS

$Y \propto M^A \pi_m^B r_n^C G_{pn}^D \delta_p^E \delta_n^F$

Y	M/r_n	A	B	C	D	E	F
R_{CSN}	0	−1	−1	—		1	−1
	$\gg 1$	0	−1	−1	−1	0	0
C_{CPN}	0	1	0	—	—	2	0
	$\gg 1$	2	0	−1	1	1	1
G_{CPN}	Any	0	1	0	1	0	0
C_{CSN}	Any	2	0	0	1	1	1

When the last term can be neglected, the result yields the approximate relations

$$C_{\theta SN}^{-1} \simeq -2A^2 G_{\theta PN} \tag{76}$$

and

$$R_{\theta SN} \simeq -2A^2 C_{\theta PN} \tag{77}$$

Here, of course, $2A^2 \equiv (G_{WPN} C_{WSN})^{-1} \equiv R_{WSN}/C_{WPN}$. Equations (76) and (77) are satisfied exactly by the final forms of the constant quantities, those where the subscript transformation $\theta \to C$ is made. These results suggest that examination of the ratios

$$U_1 \equiv -(G_{\theta PN}/G_{WPN})/(C_{\theta SN}^{-1}/C_{WSN}^{-1}) \tag{78}$$

and

$$U_2 \equiv -(C_{\theta PN}/C_{WPN})/(R_{\theta SN}/R_{WSN}) \tag{79}$$

which both should be near unity over an appreciable Ω range, should be of some interest.

It is of especial interest to point out that eqns. (70) and (73) show that C_{CPN} and R_{CSN} are both zero when

$$H_{pn}(\delta_n \delta_p)^{-1} = (M/g_s) \tag{80}$$

We may thus expect that $C_{\theta PN}$ and $R_{\theta SN}$ will also be zero near this value. In the $r_p = 0$, $r_n \gg 1$ situation with $\pi_m \ll 1$, this condition becomes approximately

$$\delta_p \delta_n^{-1} = \pi_z^{-1} \cong (M/g_n) \simeq (2M/r_n) \tag{81}$$

Therefore, when $r_n \simeq 2\pi_z M$, one may expect $C_{\theta PN}$ and $R_{\theta SN}$ to pass through zero. Although this zero point, where $C_{KN} = C_{WPN}$ and $R_{iN} = R_{WSN}$, yields perfect Warburg response for C_{KN} and R_{iN} to the degree that $C_{\theta PN} \cong C_{CPN}$ and $R_{\theta SN} \cong R_{CSN}$, Z_{iN} is not exactly equal to Z_{WN} here since the small quantities $G_{\theta PN}$ and $C_{\theta SN}^{-1}$ are not exactly zero as well. At $r_n \simeq 2\pi_z M$, Z_{iN} will, however, be closest to showing perfect Warburg response. It is interesting that such maximal Warburg response does not occur at $r_n = \infty$, where one would expect an infinite electrode reaction rate, but at a finite value of r_n.

Next, the apparent intensive–extensive character of G_{CP}, C_{CS}^{-1}, R_{CS}, and C_{CP} needs examination. Since G_{WP} and C_{WS} are intensive, eqns. (69) and (74) show that $G_{CP} \propto G_\infty \propto l^{-1}$ and $C_{CS}^{-1} \propto (M^2 C_g)^{-1} \propto l^{-1}$. These quantities are thus clearly not intensive, but it will shortly be shown that they make no significant contribution to G_{PN} and C_{iN} in the Warburg region when $\pi_m \ll 1$; thus their failure to be intensive is not important here.

On the other hand, C_{CP} and R_{CS} do play important roles. Because of eqn. (77), we need examine only C_{CP} for dependence on l. When $g_s = \infty$, eqn. (70) shows that $C_{CP} \propto MC_g$, a properly intensive quantity. The second part of C_{CP}, dominant when $(M/g_s) \gg 1$, is proportional to $M^2 C_g G_{pn}/g_s$, however. If r_p and r_n are themselves independent of l, as was tacitly assumed in the preliminary note on this work[35], then this second part is proportional to l and is therefore strongly extensive.

The normalized Chang–Jaffé boundary parameters r_p and r_n require further consideration, however. They have been introduced into the theory[4] through relations such as

$$I_p(l) = (ez_p)(r_p D_p/l)[p(l) - p_e(l)] \tag{82}$$

and

$$I_n(0) = (ez_n)(r_n D_n/l)[n(0) - n_e(0)] \tag{83}$$

Here $I_p(l)$ is the conduction current of positively charged carriers at the right electrode; $I_n(0)$ is that associated with negative carriers at the left electrode; $p(l)$ and $n(0)$ are boundary charge concentrations; and the subscript "e" denotes equilibrium values. In the present a.c. solution for the intrinsic-conduction case of no static fields within the material, $p_e \equiv p_i$, $n_e \equiv n_i$, and eqns. (82) and (83) reduce to the a.c.-only results[4]

$$I_{p_1}(l) = (ez_p)\xi_p p_1(l) \tag{84}$$

and

$$I_{n_1}(0) = (ez_n)\xi_n n_1(0) \tag{85}$$

where the effective rate constants are

$$\xi_p \equiv (D_p/l) r_p \tag{86}$$

and

$$\xi_n \equiv (D_n/l) r_n \tag{87}$$

Each ξ can be separately associated with a thermally activated rate process involving a symmetric free energy barrier to charge transfer at the electrode[22,23]. Under these conditions, ξ_p and ξ_n are never actually either zero or infinite, but their possible range is such that the r's may be well approximated by either zero or infinity. Note that we have followed Beaumont and Jacobs[22] rather than Friauf[23] in writing r_p and r_n rather than $2r_p$ and $2r_n$ in (82) and (83). Thus the present r_p and r_n are twice Friauf's r_p and r_n and agree with Beaumont and Jacobs' equivalent parameter ρ as well as the original Chang–Jaffé parameters. The present usage is slightly unfortunate, however, since it leads to definitions such as $g_p \equiv 1 + (r_p/2)$ rather than the simpler $g_p \equiv 1 + r_p$, but it has been widely enough used that it does not seem worthwhile to redefine r_p and r_n at this stage.

Now since ξ_p and ξ_n are clearly intensive quantities, eqns. (86) and (87) show that r_p and r_n are extensive! The virtue of using r_p and r_n in normalized solutions of the general (r_p, r_n; π_m, π_z; 0, M) situation is, however, that they are dimensionless and no separate knowledge of l, D_n, and D_p values is required for a normalized solution. Now it is clear that while M/r_n and M/r_p are purely intensive, quantities such as M/g_s, G_{pn}, and H_{pn}, which involve g_n and g_p, contain parts independent of l as well as parts directly involving l. Thus, even the introduction of eqns. (86) and (87) into the full expression for Z_i will not make it entirely intensive. It is thus not a pure interface impedance under all conditions.

Let us next consider, however, the usual situation of interest when electrode charge transfer occurs, that where $\varepsilon_n r_p$ or $\varepsilon_p r_n$ is much greater than unity. Then $G_{pn} \cong 1$, $g_s \cong 0.5(\varepsilon_n r_p + \varepsilon_p r_n) \gg 1$, $H_{pn} \cong g_z^2/(g_p - g_n)^2 = [(\delta_n r_p + \delta_p r_n)/(r_p - r_n)]^2$, and eqn. (80) becomes

$$(\varepsilon_n r_p + \varepsilon_p r_n)[(\delta_n r_p + \delta_p r_n)/(r_p - r_n)]^2 \cong 2M\delta_n\delta_p \tag{88}$$

For arbitrary π_m and $r_p \sim 0$, $r_n \gg 1$, for example, this zero condition becomes

$$(\varepsilon_n r_p + \varepsilon_p r_n) \cong 2M\pi_z \tag{89}$$

in agreement with (81) when $\pi_m \ll 1$. Note that eqn. (88) is entirely intensive when eqns. (86) and (87) are used for r_n and r_p.

Now for the present $g_s \gg 1$, arbitrary π_m situation, R_{CS} becomes

$$R_{CS} \cong (\varepsilon_n \varepsilon_p)^{-1} \left[\left(\frac{2}{\varepsilon_n r_p + \varepsilon_p r_n} \right) - (M\delta_n\delta_p)^{-1} \left(\frac{\delta_n r_p + \delta_p r_n}{r_p - r_n} \right)^2 \right] R_\infty \tag{90}$$

Let us now examine the case where the clearly intensive negative part of this expression is negligible compared to the positive part. Then on using

$$(R_\infty/\varepsilon_n\varepsilon_p) = (2l/e)[(\mu_p + \mu_n)/\mu_p\mu_n](z_n n_i + z_p p_i)^{-1} \tag{91}$$

and eqns. (86) and (87), one finds that

$$R_{CS} \cong \frac{(4kT/e^2)}{(z_n n_i + z_p p_i)(z_n \xi_n \varepsilon_p^2 + z_p \xi_p \varepsilon_n^2)} \tag{92}$$

This entirely intensive result holds, provided the positive part of R_{CS} remains dominant, for any π_m and either $r_n \gg 1$, $0 \leqslant r_p \ll r_n$ or $r_p \gg 1$, $0 \leqslant r_n \ll r_p$. Note that its calculation requires values of z_n and z_p, not just their ratio, π_z. Further, this expression for R_{CS} has been derived for a two-electrode situation; it must be halved when only a single working electrode is considered.

Equations (82)–(85) are similar to those used in conventional supported electrolyte theory; thus a comparison of effective rate constants is of interest. Note that in the region around equilibrium, where the present linearized results particularly apply, quantities such as the p_1 and n_1 of eqns. (84) and (85) are directly proportional to the amplitude of the applied a.c. potential, in consonance with supported case results[38].

In the conventional analysis, it is somewhat unusual to consider together both positive and negative charged entities which can react simultaneously at the electrode. But this is the general situation considered here when both r_p and r_n are non-zero. The usual expression for R_θ for a single charge carrier reacting at an electrode may be written[39] $R_\theta=(kT/nei_0)$, where i_0 is the apparent exchange current density. In the present case, we must introduce such a current for each reacting entity. Since the overall currents are in parallel and are assumed non-interacting, the effective R_θ may be written for the case of two identical electrodes as

$$R_\theta=(2kT/e)[(z_p i_{0p})+(z_n i_{0n})]^{-1} \tag{93}$$

Now in the present case of zero direct current, i_{0p}, for example, may be expressed as[40,41] $z_p e k_p c_{pe}$, where k_p is the apparent standard heterogeneous rate constant for the positive charges, and the effective concentration c_{pe} is often given by $c_O^\alpha c_R^{1-\alpha}$. Here c_O and c_R are, as before, bulk concentrations of the oxidizing and reducing species and α is the transfer coefficient. We may now write

$$R_\theta=(2kT/e^2)[z_p^2 k_p c_{pe})+(z_n^2 k_n c_{ne})]^{-1} \tag{94}$$

The predictions of eqn. (94) are different in general from those of eqns. (73) and (92) for the coupled-case R_{CS}. For example, the present unsupported treatment involves the ratio of the mobilities of the charged particles, while the extended conventional result does not. This difference between R_{CS} and R_θ certainly arises from the strong coupling between charges of opposite sign in the unsupported situation.

When eqns. (92) and (94) are set equal and $z_p p_i=z_n n_i$ is used, one finds

$$(z_p^2 k_p c_{pe}+z_n^2 k_n c_{ne})=(z_p^2 \xi_p p_i \varepsilon_n^2+z_n^2 \xi_n n_i \varepsilon_p^2) \tag{95}$$

Now when ξ_p and k_p are both zero, (95) leads to

$$\xi_n=(c_{ne}/n_i)\varepsilon_p^{-2}k_n \tag{96}$$

This result applies in the general $(0,\ r_n;\ \pi_m,\ \pi_z;\ 0,\ M)$ case with $r_n \gg 1$. When $\pi_m \ll 1$, ε_p^{-2} in (96) is essentially unity. We then see that when $c_{ne}=n_i$ as well, $\xi_n=k_n$. A result analogous to (96) can be derived in the $r_p>0$, $r_n=0$ case. Finally, it should be noted that the comparisons represented by eqns. (95) and (96) only turn out so simple when the negative second term in R_{CS} is negligible. There is clearly a contribution to R_{CS} in the present work which does not appear in the analogous R_θ of the unsupported case. Again, this term probably arises because of charge coupling effects in the unsupported case. Since it involves a negative resistance, the electrode is more open (less blocking) when $r_n=\infty$ and this term is dominant than it is when eqn. (80) holds, $g_s<\infty$, and $R_{CS}=0$.

Finally, when k_p and k_n are both non-zero, we may patch together an expression for the appropriate A_0 in this generalized supported case for comparison with the unsupported result of eqn. (42). Let us consider the situation where there is a large reservoir of neutral forms of the mobile positive and negative ions at (and in) the electrodes. The neutral concentrations will be taken large enough to be essentially invariant: small a.c. perturbations change these concentrations only negligibly, and they will not contribute significantly to the expression for A_0 in the supported case[42]. Take p_i and n_i as usual as the concentrations of the two ionic species in the bulk of the electrolyte or solid material. Then the two conventional contributions to the Warburg admittance arising from these charges are uncoupled and add directly. For the two-electrode case, the expression

$$A_0 \simeq [(e^2/2^{\frac{1}{2}}kT)\{z_p^2 p_i D_p^{\frac{1}{2}} u_0(k_p) + z_n^2 n_i D_n^{\frac{1}{2}} u_0(k_n)\}]^{-1}$$
$$= [(e^2/2^{\frac{3}{2}}kT)(z_p p_i + z_n n_i)\{z_p D_p^{\frac{1}{2}} u_0(k_p) + z_n D_n^{\frac{1}{2}} u_0(k_n)\}]^{-1} \quad (97)$$

then seems appropriate. Here $u_0(x)$ is the unit step function: $u_0(x \leqslant 0) = 0$; $u_0(x > 0) = 1$. The introduction of this function is probably an approximation (associated with the assumption of no coupling at all), but it is needed, just as is the function G_{pn}, which appears in eqns. (31) and (42) for A and A_0 and in all unsimplified expressions such as eqns. (69), (70), (73) and (74). When $r_p = r_n$, $G_{pn} = 0$, so A and A_0 go to infinity in this completely blocking case.

The present supported A_0 is still quite different, however, from the unsupported case result of eqn. (42). There, when one D is much smaller than the other, that one dominates the expression for A_0. Here, when $z_p D_p^{\frac{1}{2}} u_0(k_p) \gg z_n D_n^{\frac{1}{2}} u_0(k_n)$, for example, only the larger D is important in A_0. Even when $z_n = z_p \equiv z_e$, $n_i = p_i \equiv c_i$, $D_p = D_n \equiv D_e$, and k_p, $k_n > 0$, the unsupported result is, from eqn. (43), $A_0 \cong 2^{\frac{3}{2}} kT/e^2 z_e^2 c_i D_e^{\frac{1}{2}}$, while the result following from eqn. (97) is one fourth of this A_0. The differences between the unsupported and supported results again arise from the charge coupling present in the unsupported case and perhaps also from some possible inappropriateness of eqn. (97). It does, however, seem very reasonable that the magnitude of the Warburg impedance be appreciably higher, as above, in the unsupported than in the supported situation. Finally, although the present theory and results have been here applied primarily in an electrochemical context, they also apply to solids as well. Impurity ions and various charged defects in crystals may be the dominant charge carriers, and electrode kinetics may involve injection and annihilation of defects as well as electron (and hole) transfer and chemical reactions at the electrodes.

B. Approximate equivalent circuits

Figure 20a shows the conventional equivalent circuit usually employed over the entire frequency region for both supported and unsupported electrolyte situations[37,43,44]. The Z_W here is usually taken to involve the A_0 of eqn. (50), rewritten for a single working electrode, or a simplification of it. The element C_d is the double-layer capacitance. The usual expression for C_d in the case of two identical plane-parallel electrodes is $MC_g = \varepsilon/8\pi L_D$, where L_D here involves the concentrations of all mobile charges completely blocked at the electrodes. Finally, R_θ is the equilibrium charge transfer resistance discussed in Part A of this Section; it will be zero for infinite electrode reaction rates. All quantities in this circuit are intensive except the extensive R_∞. Here the other extensive quantity, C_g, has been omitted[45]. Figures 20b and 20c show the limiting forms of the circuit when $\omega \to 0$ and $\omega \to \infty$, respectively. Note that although the circuit is supposed to apply to a faradaic process, it does not allow a continuous current to flow as it should[35,46] and as the circuits of Fig. 1 do.

Let us now consider how the circuits of Fig. 1, representing the unsupported situation, simplify for $\pi_m \ll 1$ when the relations of Section VI-A for Y_i and Z_i are used in the approximate Warburg region. The results thus only apply when $r_p \neq r_n$. Figure 21a is a form of Fig. 1a in which exact Warburg elements are shown explicitly. Now consider the situation (0, r_n; π_m, π_z; 0, M) when $\pi_m \ll 1$ and $r_n \gg 1$. Then $G_E \cong G_\infty$, $G_D = [\varepsilon_n r_n/(r_n+2)]G_\infty$, and $G_{\theta P} \cong G_{CP} = -[\varepsilon_p \varepsilon_n \{r_n/(r_n+2)\}^2]G_\infty$. Since

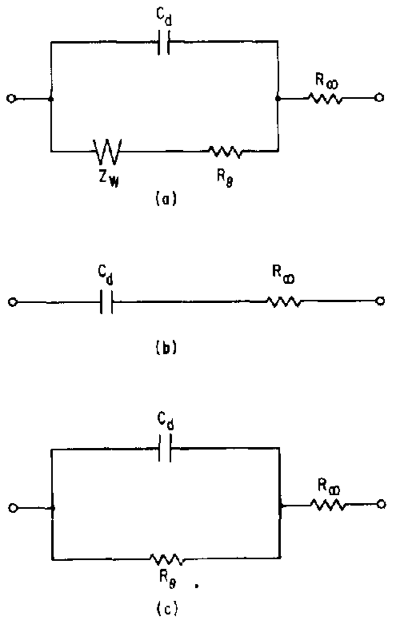

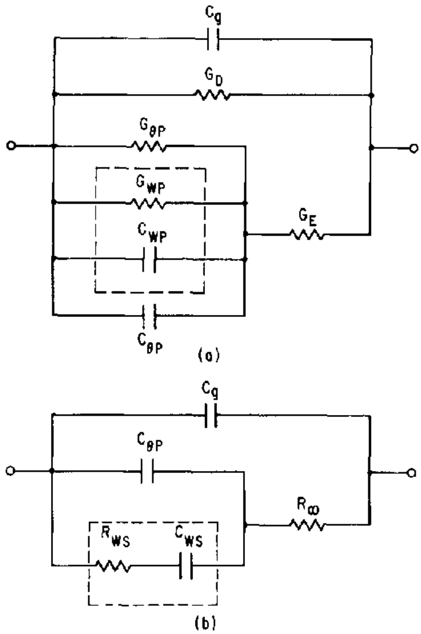

Fig. 20. (a) Conventional electrochemical equivalent circuit; (b) low-frequency-limiting form of the circuit; (c) high-frequency-limiting form of the circuit.

Fig. 21. (a) Form of the exact equivalent circuit of Fig. 1 appropriate in the Warburg frequency response region. (b) Approximate but frequently applicable form of the circuit.

$\varepsilon_p \cong 1$ and $\varepsilon_n \cong \pi_m$, G_{DN} and $|G_{\theta PN}|$ are much smaller than unity. It will thus make little difference if $G_{\theta P}$ is reconnected to the right terminal of G_E rather than the left. Then G_D and $G_{\theta P}$ are in parallel, and their sum is approximately $\pi_m[r_n/(r_n+2)][1-\{r_n/(r_n+2)\}]G_\infty = [2\pi_m r_n/(r_n+2)^2]G_\infty$. For $\pi_m \ll 1$ and $r_n \gg 1$, the result is completely negligible, thus justifying the absence of G_D in the conventional circuit when applied to an unsupported situation: (a) in the Warburg region only, and (b) when $\pi_m \ll 1$.

The result of the above manipulations is shown in Fig. 21b. Note the absence of any direct current path from electrode to electrode in this Ω region, region B of Table 2. Under some usual conditions, we may still simplify the circuit of Fig. 21b further. The reactance of $C_{\theta P}$ is $(\omega C_{\theta P})^{-1} \equiv R_\infty/\Omega C_{\theta PN} \cong (\Omega C_{CPN})^{-1}R_\infty$. Taking, for example, $\Omega = 0.1\,\pi_m$ and assuming $(\delta_n\delta_p M/g_s) \gg H_{pn}$, one finds $|\Omega C_{CPN}|^{-1}R_\infty \simeq (10g_s/\delta_n\delta_p M)(\pi_m M)^{-1}G_{pn}^{-1}R_\infty \cong (10g_s/\delta_n\delta_p M)(\pi_m M)^{-1}R_\infty$. Since $\pi_m M \ll 1$, this result will appreciably exceed R_∞ provided $H_{pn} \ll (\delta_n\delta_p M/g_s) \ll 10(\pi_m M)^{-1}$, a quite practical situation. Then, and for smaller Ω values, it will be an adequate approximation to reconnect $C_{\theta P}$ to the right end of R_∞, and the circuit of Fig. 22a is obtained.

Another approximate equivalent circuit appropriate for $\pi_m \ll 1$ may be obtained by introducing the results of eqns. (64) and (65) in Fig. 1a. One then obtains the circuit of Fig. 22b. On ignoring $R_D \sim \pi_m^{-1}R_\infty$, replacing $R_E \cong R_\infty$ with R_∞, and ignoring $C_{\theta S}^{-1}$ compared to C_{WS}^{-1}, the circuit of Fig. 22c is obtained. This

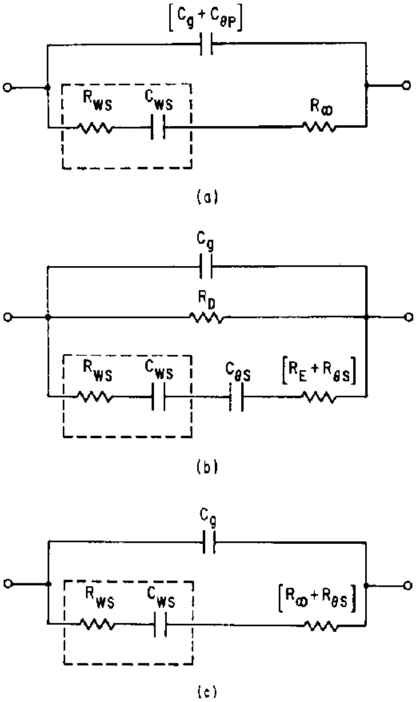

Fig. 22. (a) A more approximate form of the circuit of Fig. 21b; (b) an alternate form of the exact equivalent circuit of Fig. 1 appropriate in the Warburg region; (c) approximate form of the (b) circuit.

circuit is probably not quite as accurate as those of Fig. 21b and 22a since R_D was ignored, not "cancelled".

Comparison of the circuits of Figs. 20a, 21b, 22a, and 22b shows both similarities with and differences from the conventional circuit. In Fig. 22a, $C_g + C_{\theta P} \cong C_{\theta P}$ plays the role of the C_d of Fig. 20a. But note that the maximum positive value of $C_{\theta P} \simeq C_{CP}$ applicable for $r_p = 0$ and $r_n = \infty$, is about $M\delta_p^2 C_g$, always less than MC_g. When "C_d" is actually determined in the unsupported case from measurements in the plateau region (region C of Table 2; see also Fig. 17), the result is not MC_g anyway but is $C_{PS} \cong M\delta_p^{\frac{1}{2}} C_g$, still always greater than $M\delta_p^2 C_g$. Thus $C_{\theta P}$ is never exactly the double-layer or even the plateau capacitance. More important, eqn. (70) shows that $C_{\theta P} \cong C_{CP}$ can go negative, and its maximum magnitude for $(M/g_s) \gg 1$ can greatly exceed MC_g.

Similarly, the $R_{\theta S}$ element of Fig. 22c may be taken to play the role of the charge transfer resistance of Fig. 20a. Note that $C_{\theta P}$ and $R_{\theta S}$ are not independent, however, as shown by eqn. (77). When one is positive, the other is negative. In the $r_p \neq \infty$, $r_n = \infty$ case, eqn. (73) shows that $R_{\theta S} \simeq R_{CS} = R_{CSN} R_\infty$ is negative. Similarly when $(M/g_s) \gg 1$, R_{CS} is positive with dominant part $(G_{pn}\varepsilon_n\varepsilon_p g_s)^{-1} R_\infty$. In the present $\pi_m \ll 1$ case, $\varepsilon_n^{-1} \cong \pi_m^{-1} \gg 1$; thus, this term will greatly exceed R_∞. Note that the ratio R_∞/g_s will be very nearly intensive if $r_n \gg 2$ but will be neither purely intensive nor extensive when this condition does not hold, *i.e.* in the case of a very slow electrode reaction. Finally, it is important to note that $C_{\theta P}$ and $R_{\theta S}$ do not

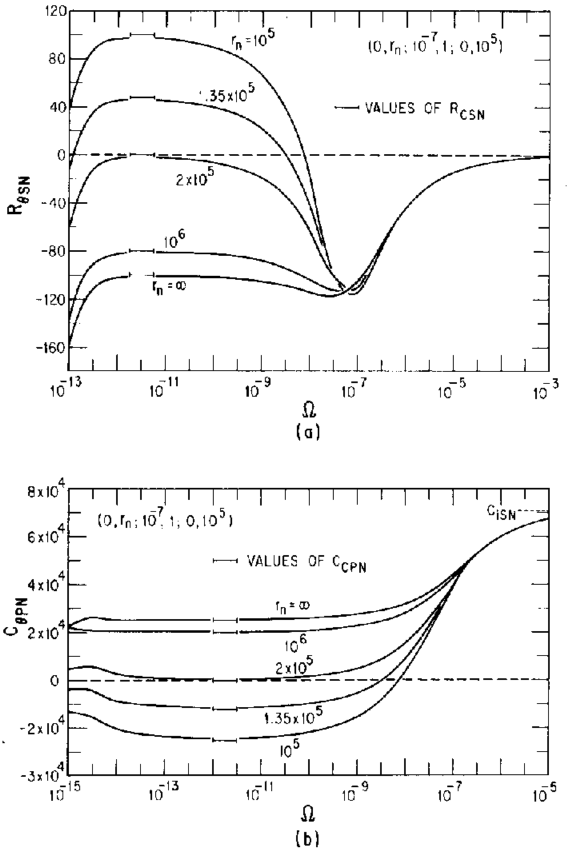

Fig. 23. Normalized frequency dependence of the electrode-reaction quantities $R_{\theta SN}$ and $C_{\theta PN}$ for the $(0, r_n; 10^{-7}, 1; 0, 10^5)$ situation.

appear simultaneously in the same equivalent circuit as do the C_d and R_θ of Fig. 20a.

Figure 23 shows how $R_{\theta SN}$ and $C_{\theta PN}$ actually depend on Ω for the $(0, r_n; 10^{-7}, 1; 0, 10^5)$ case. These quantities were calculated essentially exactly by the computer rather than from the approximations of eqns. (67) and (71). We see that $R_{\theta SN}$ and $C_{\theta PN}$ are substantially constant up to $\Omega \sim (\pi_m/30)$ but do not remain constant close to the lower Warburg region boundary of 40 $\pi_m M^{-2}$, here at $\Omega = 4 \times 10^{-16}$. Figure 23a shows that $R_{\theta SN} \to 0$ as $\Omega > \pi_m$. Actually, in this region $R_{\theta SN} \cong -R_{WSN}$, so $R_{iN} \equiv R_{WSN} + R_{\theta SN}$ approaches zero rapidly. For example at $\Omega = 10^{-5}$, $R_{WSN} = 10\sqrt{2}$ and $R_{iN} \cong 6.1 \times 10^{-3}$. Note that there is not much of a C_{PS} plateau region here since $\pi_m M$ is not sufficiently small. There is, of course, a wider plateau for C_{iN}, and we see in Fig. 23b $C_{\theta PN} \to C_{iSN}$ as $\Omega \gtrsim 10^{-8}$ or so. Since the susceptance of $C_{\theta P}$ will be much greater than the admittance of Z_W as Ω appreciably exceeds π_m, the circuit of Fig. 21b approaches the plateau circuit of Fig. 17 as it should in this plateau region. Similarly, the circuit of Fig. 22b also goes to that of Fig. 17 as Ω increases since $R_i \to 0$ and $C_i = (C_{WS}^{-1} + C_{\theta S}^{-1})^{-1}$ approaches C_{iS}.

In order to present further information on the important quantities $C_{\theta PN}$,

TABLE 4

VALUES OF CIRCUIT ELEMENTS MULTIPLIED BY g_s FOR THE $(0, r_n; 10^{-7}, 1; 0, 10^5)$ SITUATION

Range values give 10 percent variation values of Ω on a logarithmic basis

r_n	*Constant quantities*		*Frequency-dependent quantities*			
	$g_s R_{CSN}$	$-g_s C_{CPN}$	$Max(g_s R_{\theta SN})$	$log_{10}\Omega$ range min/max	$Min(-g_s C_{\theta PN})$	$log_{10}\Omega$ range min/max
2×10^6	-9.000×10^7	-2.250×10^{10}	-9.10×10^7	$-12.4/-8.6$	-2.26×10^{10}	$-14.6/-9.0$
2×10^5	1.001	2.502×10^2	-1.92×10^5	$-11.7/-11.2$	-3.72×10^7	$-12.2/-11.4$
2×10^4	9.002×10^6	2.250×10^9	8.93×10^6	$-13.1/-9.5$	2.20×10^9	$-14.1/-10.3$
2×10^3	9.920×10^6	2.470×10^9	9.88×10^6	$-13.8/-9.8$	2.32×10^9	$-14.4/-11.8$
200	1.019×10^7	2.448×10^9	1.02×10^7	$-14.4/-10.6$	2.02×10^9	$-14.8/-13.3$
20	1.210×10^7	2.066×10^9	1.21×10^7	$-15.1/-11.6$	1.23×10^9	$-15.3/-14.6$

C_{CPN}, $R_{\theta SN}$, and R_{CSN}, Tables 4 and 5 show their variation under different conditions. Table 4 applies for the same $(0, r_n; 10^{-7}, 1; 0, 10^5)$ situation presented in Fig. 23 but extends to much smaller r_n values and thus into the very slow electrode reaction region. All element values in Table 4 are multiplied by g_s in order to remove first order variation arising from g_s changes. Here $g_s \cong g_n = 1 + (r_n/2)$ to excellent approximation. The Table gives the approximate maximum values of $g_s R_{\theta SN}$ and minimum values of $-g_s C_{\theta PN}$ for comparison with $g_s R_{CSN}$ and $-g_s C_{CPN}$. In addition the Table presents the Ω ranges over which $R_{\theta SN}$ remains within 10 percent of its maximum value and $C_{\theta PN}$ remains within 10 percent of its minimum. The ranges are shown in logarithmic form as $(\log_{10}\Omega_{min})/(\log_{10}\Omega_{max})$ where Ω_{min} and Ω_{max} are the lower and upper 10 percent points.

Table 4 shows that when r_n is appreciably smaller than the $2M$ cross-over value, the quantities shown remain nearly constant for more than a 100-times reduction in r_n. When $(r_n/2M) \lesssim 10^{-4}$, however, such constancy disappears. Incidentally, $(R_{\theta SN})_{max}$ values occur here at $\Omega \simeq 10^{-12}(10\, r_n/2M)^{\frac{1}{2}}$. For $(r_n/2M) < 0.1$, $(C_{\theta PN})_{min}$ values appear at $\Omega \simeq 10^{-11}(r_n/2M)$. Thus at $r_n = 2\times10^3$, these Ω values are approximately 3×10^{-13} and 10^{-13}. The ranges given show that in the approximate constant region $R_{\theta SN}$ remains close to its maximum value for 3 or 4 decades, and $C_{\theta PN}$ shows a decreasing ±10 percent range as r_n decreases below $0.2M$. Incidentally, for $(0, 2\times10^3; 10^{-7}, 1; 0, 10^5)$ the quantity U_1 shows a ±10 percent $\log_{10}\Omega$ variation range around a value of unity of -14.75 to -12.7 and increases monotonically with Ω in this range. On the other hand, U_2 shows a range of -13.9 to -12.2 for 10 percent variation around the value of unity and decreases monotonically with increasing Ω.

Table 5 is similar to Table 4 except that here $(r_n/2M)$ is fixed at the value 10^{-2} and thus both r_n and M vary. In addition, although g_s is again used to multiply the resistive elements, M^{-1} is used in its place for the capacitative ones. Here we see quite good constancy of the elements shown nearly down to $r_n = 20$. Note that the $\log_{10}\Omega$ ranges decrease for both quantities as r_n and M decrease, but most of the decrease arises from a decrease in magnitude of the low-Ω boundary value associated with the M reduction. Here $(R_{\theta SN})_{max}$ values occur at $\Omega \simeq 10^{-7.5}\ M^{-1}$ and $(C_{\theta PN})_{min}$ values at $\Omega \simeq 10^{-8}\ M^{-1}$. For $(r_n/2M) = 10^{-2}$. R_{CSN} itself increases

TABLE 5

VALUES OF NORMALIZED CIRCUIT ELEMENTS FOR THE $(0, r_n; 10^{-7}, 1; 0, 50r_n)$ SITUATION

Ranges defined as in Table 4

r_n	M	*Constant quantities*		*Frequency-dependent quantities*			
		$g_s R_{CSN}$	$-M^{-1} C_{CPN}$	$Max(g_s R_{\theta SN})$	$log_{10}\Omega$ range min/max	$Min(-M^{-1} C_{\theta PN})$	$log_{10}\Omega$ range min/max
2×10^5	10^7	9.900×10^6	24.749	9.90×10^6	$-16.4/-9.9$	24.59	$-18/-12.2$
2×10^4	10^6	9.902×10^6	24.743	9.89×10^6	$-15.1/-9.8$	24.24	$-16.1/-12$
2×10^3	10^5	9.920×10^6	24.676	9.88×10^6	$-13.8/-9.8$	23.14	$-14.4/-11.8$
200	10^4	1.010×10^7	24.020	9.97×10^6	$-12.4/-9.8$	19.75	$-12.8/-11.1$
20	10^3	1.197×10^7	18.577	1.12×10^7	$-11.1/-9.7$	10.75	$-11.3/-10.6$

here from about 99 to 1.2×10^6 as r_n decreases from 2×10^5 to 20. Thus, in this entire range $R_{CS} \gg R_\infty$, and the reaction resistance dominates the bulk resistance. Over this same range, C_{CP} remains approximately equal to $-24\ MC_g$, much larger in magnitude than the corresponding double-layer capacitance.

C. Warburg data analysis

There are two principal ways Warburg-region data are usually presented either as impedance or admittance components. In the impedance case, the real and imaginary parts of Z_T (or here more properly Z_i) are plotted *versus* $\omega^{-\frac{1}{2}}$ to yield approximate straight lines. In the present $\pi_m \ll 1$ case, over much of the range of interest where $Z_{TN} \cong Z_{iN}+1$ and $Z_{iN} \gg 1$, either Z_T or Z_i may be used, but it is better to eliminate R_∞ whenever possible as is usually done, either correctly or incorrectly, in electrochemical situations.

We shall use normalized variables in plotting Z_i here since their use will make the results more independent of M and π_m. Let the frequency variable be

$$X \equiv 2^{\frac{1}{2}}(AM\Omega^{\frac{1}{2}})^{-1} \equiv 2^{\frac{1}{2}}(MA^2)^{-1}R_{WSN} \equiv 2^{\frac{1}{2}}M^{-1}C_{WSN} \tag{98}$$

When $\pi_m \ll 1$, $\pi_z = 1$, and $G_{pn} \cong 1$, $X \cong [\Omega(2+\pi_m+\pi_m^{-1})]^{-\frac{1}{2}} \cong (\pi_m/\Omega)^{\frac{1}{2}}$. Next, further normalize the impedance to NZ_{iN}, where

$$N \equiv (2/10MA^2) \tag{99}$$

The numerical values $2^{\frac{1}{2}}$, 2, and 10 in these quantities are arbitrary scaling factors. We may now write, on using eqn. (64) and replacing $R_{\theta SN}$ by R_{CSN},

$$\begin{aligned} NR_{iN} &\simeq NR_{CSN}+(2^{\frac{1}{2}}X/10) \\ &= -0.4M^{-1}C_{CPN}+(2^{\frac{1}{2}}X/10) \\ &= 0.4G_{pn}[\delta_n\delta_p(M/g_s)-H_{pn}]+(2^{\frac{1}{2}}X/10) \end{aligned} \tag{100}$$

Similarly, on replacing $C_{\theta SN}$ by C_{CSN} and using eqn. (65), we find

$$\begin{aligned} N(\Omega C_{iN})^{-1} &\simeq N(\Omega C_{CSN})^{-1}+(2^{\frac{1}{2}}X/10) \\ &= (10G_{pn}\delta_n\delta_pM)^{-1}X^2+(2^{\frac{1}{2}}X/10) \cong (2^{\frac{1}{2}}X/10) \end{aligned} \tag{101}$$

Figure 24 shows curves of this kind for $r_p \sim 0$, $r_n = \infty$. The points, appropriate for $\pi_m = 1$, show how little the curves change on going from $\pi_m \ll 1$ or $\pi_m \gg 1$ to $\pi_m = 1$. The slopes agree with those above, and the $X=0$ intercept for NR_{iN} is, from eqn. (100), $-0.4G_{pn}H_{pn} = -0.4\delta_p^2 = -0.1$. The actual intercept shown is slightly larger in magnitude. The capacitative reactance curve extrapolates to the origin, in agreement with eqn. (101) and with most experimental results. Note that for the present case, since $\Omega \cong \pi_m X^{-2}$, these curves where $X \leqslant 10$ emphasize the Ω region near π_m. They remain substantially straight lines, nevertheless, down to $X \sim 2$, where $\Omega \sim \pi_m/4$. Curves of this sort for series capacitance and resistance are frequently found experimentally[37,44,47–53], but usually the R_i curve lies above the other (*i.e.* $R_\theta > 0$). Some slight evidence of $R_\theta < 0$, as in the present $r_p \sim 0$, $r_n = \infty$ case, has, however, been published[49,51].

Turning now to the admittance approach, we may rewrite eqn. (3) as

$$Y_{TN} \equiv G_{PN}+i\Omega C_{PN} = (i\Omega+G_{DN})+(Z_{iN}+R_{EN})^{-1} \tag{102}$$

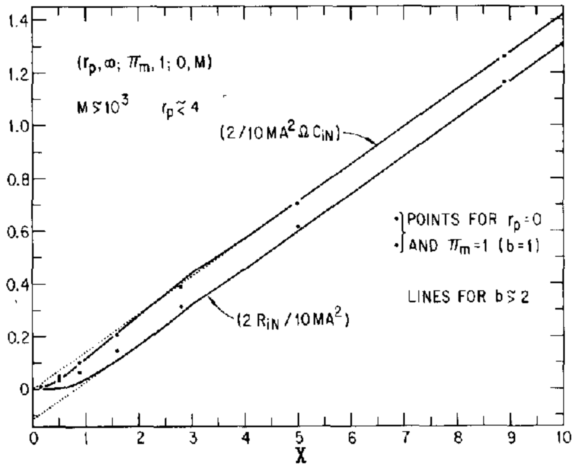

Fig. 24. The further normalized quantities $N(\Omega C_{\mathrm{iN}})^{-1}$ and NR_{iN} *versus* X for the $(r_{\mathrm{p}}, \infty;\ \pi_{\mathrm{m}}, 1;\ 0, M)$ situation. Here $N \equiv (5MA^2)^{-1}$ and $X \equiv (2/\Omega)^{\frac{1}{2}}(AM)^{-1}$.

In the $\pi_{\mathrm{m}} \ll 1$ case, where $R_{\mathrm{EN}} \cong 1$ and $|Z_{\mathrm{iN}}| \gg 1$, this equation leads, on using eqns. (58) and (63), to

$$C_{\mathrm{PN}} \cong 1 + C_{\mathrm{WPN}} + C_{\theta\mathrm{PN}} \tag{103}$$

and

$$G_{\mathrm{PN}} \cong G_{\mathrm{WPN}} + (G_{\mathrm{DN}} + G_{\theta\mathrm{PN}}) \tag{104}$$

Note that eqn. (103) is more accurate than eqn. (28) of Section V which applies to the same situation. Now we have already seen that for $\pi_{\mathrm{m}} \ll 1$, $G_{\mathrm{DN}} + G_{\theta\mathrm{PN}} \cong G_{\mathrm{DN}} + G_{\mathrm{CPN}} \cong 2\pi_{\mathrm{m}}/r_{\mathrm{n}} \sim 0$ for $r_{\mathrm{n}} \gg 1$. Thus, $G_{\mathrm{PN}} \cong G_{\mathrm{WPN}}$ here.

Now if we set $C_{\theta\mathrm{PN}} \cong C_{\mathrm{CPN}}$ and neglect the unity term on the r.h.s. of eqn. (103), the result can be written

$$\begin{aligned} M^{-1} C_{\mathrm{PN}} &\cong M^{-1} C_{\mathrm{CPN}} + (X/2^{\frac{3}{2}}) \\ &= G_{\mathrm{pn}}\{H_{\mathrm{pn}} - \delta_{\mathrm{n}}\delta_{\mathrm{p}}(M/g_{\mathrm{s}})\} + (X/2^{\frac{3}{2}}) \end{aligned} \tag{105}$$

On using the good approximation $G_{\mathrm{PN}} \cong G_{\mathrm{WPN}} \equiv \Omega C_{\mathrm{WPN}}$, one also readily finds that eqn. (103) may be rewritten as

$$\begin{aligned} C_{\mathrm{PN}} &\cong C_{\theta\mathrm{PN}} + \Omega^{-1} G_{\mathrm{PN}} \\ &\cong C_{\mathrm{CPN}} + \Omega^{-1} G_{\mathrm{PN}} \end{aligned} \tag{106}$$

In unnormalized form this equation becomes

$$C_{\mathrm{P}} \cong MG_{\mathrm{pn}}[H_{\mathrm{pn}} - \delta_{\mathrm{n}}\delta_{\mathrm{p}}(M/g_{\mathrm{s}})]C_{\mathrm{g}} + \omega^{-1} G_{\mathrm{P}} \tag{107}$$

De Levie[10] and Leonova *et al.*[54] have derived the similar result

$$C_{\mathrm{P}} = C_{\mathrm{d}} + (\omega R_{\mathrm{P}})^{-1} \tag{108}$$

which is consistent with the conventional circuit of Fig. 20a only when $R_\theta \cong 0$. Again we see, however, that plotting C_{P} *vs.* $(\omega R_{\mathrm{P}})^{-1}$ here does not yield C_{d} but rather C_{CP}. Although the above authors required the assumption $R_\theta \cong 0$ to obtain eqn. (108), the similar eqn. (107) found here does *not* require the assumption

$R_{\theta S}=0$. In fact, eqn. (77) indicates that when $C_{\theta PN} \cong C_{CPN} \neq 0$. $R_{\theta SN} \cong R_{CPN}$ cannot be zero either. Thus, experimental satisfaction of eqn. (107) does not necessarily indicate that $R_\theta=0$ and k_p or k_n is infinite.

Figure 25 shows some $\pi_m \ll 1$ curves of the form of eqn. (105). They are fully consistent with it over most of the X range and of the form found experimentally. For the present situation, eqn. (105) yields a $X \to 0$ intercept of δ_p^2. Thus the corresponding C_P intercept is $M\delta_p^2 C_g$, always less than MC_g or $M\delta_p^{\frac{1}{2}} C_g$, as mentioned earlier. The insert in Fig. 25a shows the $X \lesssim 0.6$ region in expanded form. For $X \gtrsim 1$, the curve is essentially independent of π_m for $\pi_m \lesssim (10\ M)^{-1}$.

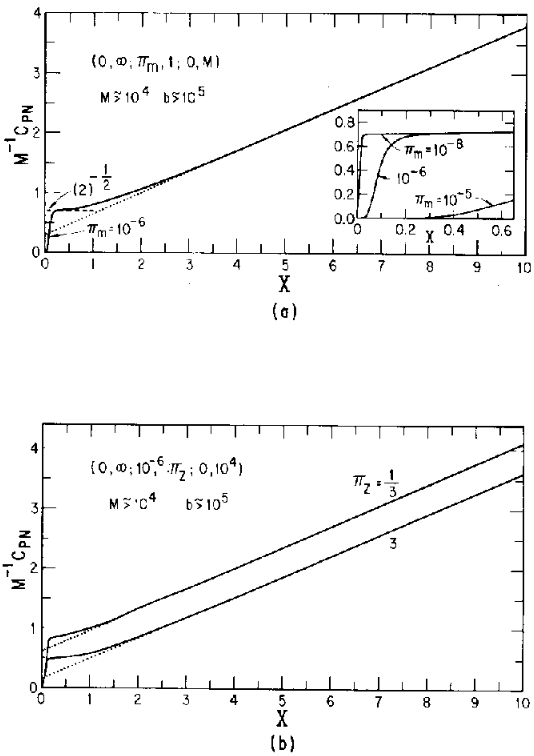

Fig. 25. The quantity $M^{-1}C_{PN}$ *versus* X for $(0, \infty; \pi_m, 1; 0, M)$ and $(0, \infty; 10^{-6}, \pi_z; 0, 10^4)$ situations.

Figure 26 is plotted for $r_n \leqslant \infty$ and may be compared to the $r_n=\infty$ results of Fig. 24. On the much extended X scale used here, the dots, corresponding to the $r_n=\infty$ condition, seem to lie virtually on the ideal Warburg line ($R_{\theta SN}=0$), because the resolution is less here than that of Fig. 24. Tables of pertinent values are shown on each part of Fig. 26. The specific values of R_{CSN} shown in the Table of Fig. 26a apply for $\pi_m = 10^{-6}$, although the curves themselves apply for $\pi_m \lesssim 0.03$.

The $X \to 0$ intercepts of Fig. 26a all lie somewhat below those that follow theoretically from eqn. (100), NR_{CSN}. The differences arise both from inaccuracies in determining the final limiting slope graphically and probably also from the approximate character of eqn. (100). Now Fig. 26b shows no large departure from

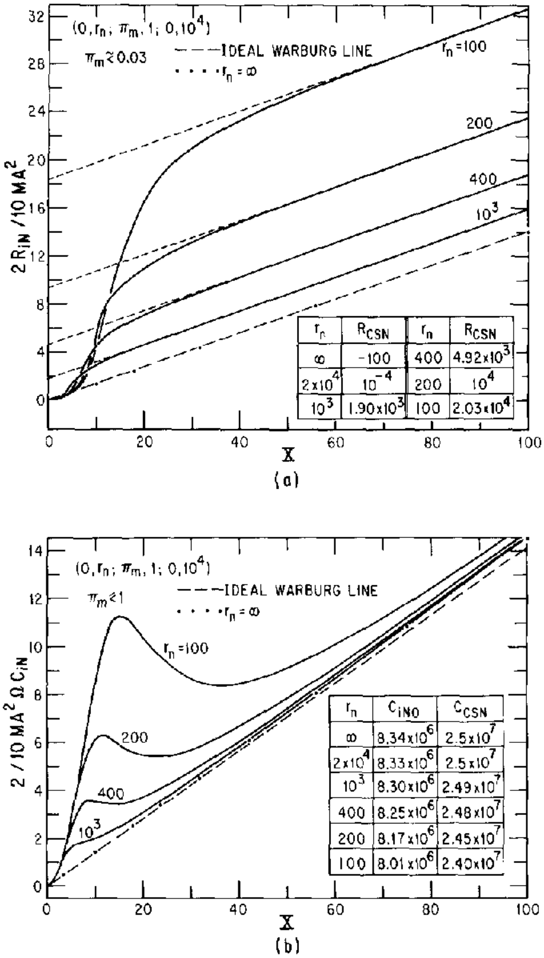

Fig. 26. The quantities NR_{iN} and $N(\Omega C_{iN})^{-1}$ *versus* X for the $(0,\ r_n;\ \pi_m,\ 1;\ 0,\ 10^4)$ situation with large values of (M/r_n).

the Warburg line as r_n is decreased down to ~ 200 (where $M/g_s \simeq 10^2$), while increases of R_{CSN} with decreasing r_n move the NR_{iN} line upward. Thus, when $(M/g_s) > (\delta_p \delta_n)^{-1} H_{pn}$ (equal to unity for $\pi_z = 1$), so that the $X \to 0$ intercept is positive, the R_i lines will then lie above the $(\omega C_i)^{-1}$ lines, as is usually observed experimentally.

It is also worth noting that the forms of the NR_{iN} and $N(\Omega C_{iN})^{-1}$ curves of Fig. 26 are very similar to those given by Vetter[56] for the components of the faradaic impedance (supported case) with diffusion and heterogeneous reaction rate control. But the present curves for NR_{iN} are quite unlike those given by Vetter for the more complicated combined case of charge transfer, diffusion, and heterogeneous reaction rate control[55].

In Vetter's diffusion and heterogeneous reaction rate control case, his faradaic impedance, which essentially corresponds to the present Z_i, involves Z_W in series with a resistance R_r and capacitance C_r, also connected in series. These elements thus correspond to the present $R_{\theta S}$ and $C_{\theta S}$ (see Fig. 22b). It is found[55] that $R_r \propto [1+(\omega/k)^2]^{-1}$ and $C_r \propto [1+(k/\omega)^2]$, where k is an effective rate constant for the reaction considered. These frequency dependences are somewhat similar to but not the same as those of $R_{\theta S}$ and $C_{\theta S}$ following from the present treatment. For example, in Fig. 23 $R_{\theta SN}$ begins to drop off rapidly with Ω at a value of Ω related much more to π_m than to ξ_n (or r_n), and it goes negative to a value determined principally by $(\pi_m M)^{-1}$ before then beginning to approach zero. It should be noted, however, that for $(r_n/2M) \lesssim 10^{-2}$, as in the $r_n = 200$ curves of Fig. 26, the maximum negative value is far smaller in magnitude than is $(R_{\theta SN})_{max} \cong R_{CSN}$. Similarly, $C_{\theta SN}$ drops off from $\sim C_{CSN}$ eventually as Ω increases toward π_m. As Ω decreases, on the other hand, $C_{\theta SN}$ reaches a maximum nearly equal to C_{CSN} and then slowly decreases toward C_{iN0}, rather than increasing indefinitely as does C_r.

It is important to emphasize, nevertheless, that it is the drop off with increasing Ω of $R_{\theta SN}$ and $C_{\theta SN}$ which leads to the behavior of the curves of Fig. 26 in the interesting region $5 \lesssim X \lesssim 35$. Incidentally, for the choice $\pi_m = 10^{-6}$, when $X \simeq 9.8$ here, $\Omega = 10^{-9}$, and $\Omega = 10^{-10}$ for $X \simeq 31$. The minima in the $N(\Omega C_{iN})^{-1}$ curves (apparent for $r_n \leqslant 400$) occur when $C_{\theta SN} \simeq C_{WSN}$. Since $C_{\theta SN}$ decreases with increasing Ω faster than C_{WSN} in this region, $C_{\theta SN}$ soon dominates the series combination, and the maxima in the reactance curves occur at $C_{\theta SN} \sim C_{WSN}/3$.

Alternatively, the curves of Fig. 26 may be interpreted in a simple fashion using eqn. (4′). The maxima in the curves of Fig. 26b are associated with the maximum value of $-\mathrm{Im}(Z_{2N})$, $(\varepsilon_n r_n)^{-1}$. The Warburg response of Z_{1N} (*not* exactly Z_{WN}) is in series with the parallel combination of $R_2 = (2/\varepsilon_n r_n)R_\infty$ and $C_2 = MC_g$. Note that when R_{CS} is dominated by its positive part, as in the present situation, and $\pi_m \ll 1$, $R_{CS} \cong (2/\varepsilon_n \varepsilon_p^2 r_n)R_\infty \cong (2/\varepsilon_n r_n)R_\infty = R_2$. Thus R_2 may be considered a pertinent equilibrium charge transfer resistance in the present unsupported case. It is interesting that in the formulation represented by eqn. (4′) such a quantity appears directly in parallel with the double-layer capacitance $C_2 = MC_g$ and thus no effect of C_2 appears at all when $r_n = \infty$!

The close correspondence of the curves of Figs. 24 and 26, first with those that are found in the supported case for diffusion and charge transfer rate control[44], then with those for diffusion and chemical reaction rate control[55] is no accident. In the $(0, r_n; \pi_m, \pi_z; 0, M)$ situation with $r_n \gg 1$, we may use eqns. (73) and (87) to allow definition of an effective rate constant, ξ_{ne}, which particularly covers the R_{CSN} region of most interest, $1 < R_{CSN} \leqslant \infty$. Let us thus write in this case,

$$R_{CSN} \equiv (2D_n/lG_{pn}\varepsilon_n\varepsilon_p^2)\xi_{ne}^{-1} \tag{109}$$

where

$$\begin{aligned}\xi_{ne}^{-1} &= (\varepsilon_p l/2D_n)[\{1+(\varepsilon_p l\xi_n/2D_n)\}^{-1} - (H_{pn}/M\delta_n\delta_p)] \\ &\cong \xi_n^{-1} - (\varepsilon_p L_D H_{pn}/\delta_n\delta_p D_n)\end{aligned} \tag{110}$$

A more exact expression for ξ_{ne} could be formed as in eqn. (109) but with $R_{\theta SN}$ replacing R_{CSN}.

Now the foregoing results show that when the first term on the r.h.s. of eqn. (110) does not dominate the expression but ξ_{ne}^{-1} remains $\geqslant 0$, R_{iN} and C_{iN} lead to results like those of simple charge transfer in the unsupported case. But when the ξ_n^{-1} term dominates, the results are like those for chemical reaction control. Evidently in the present exact treatment of the unsupported case, the two processes meld together. There is a smooth transition from apparent charge transfer control in the region $0<(\xi_n/\xi_{ne})\ll 1$ to apparent chemical reaction rate control when $(\xi_n/\xi_{ne})\lesssim 1$. Notice that the effective rate constant ξ_{ne} is more analogous to the conventional rate constant than is ξ_n, since $\xi_{ne}=\infty$ corresponds to zero electrode reaction resistance, to the degree that $R_{\theta SN}=R_{CSN}$.

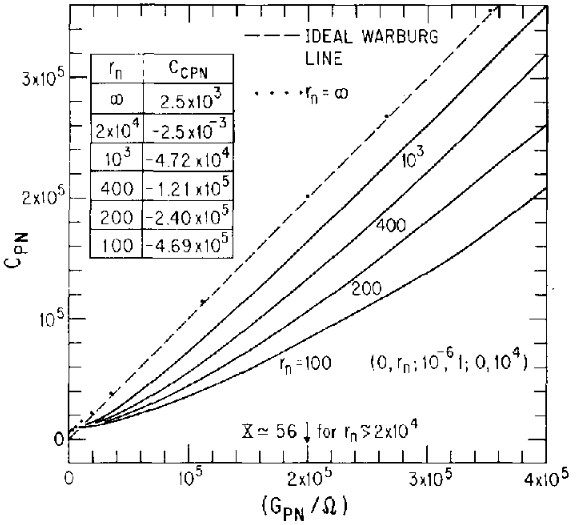

Fig. 27. The quantity C_{PN} plotted *versus* (G_{PN}/Ω) for the $(0, r_n;\ 10^{-6}, 1;\ 0, 10^4)$ situation.

Finally, Fig. 27 shows C_{PN} *versus* (G_{PN}/Ω) for various r_n values. The results are in substantial agreement with eqn. (106). Here, because $(2M/r_n)\gg 1$ for most of the curves shown, most of the C_{CPN} intercepts are negative, although positive ones would be found for r_n values satisfying $(g_s H_{pn})>(\delta_n\delta_p)M$. A specific value of X is shown at the bottom of this Figure. Its size indicates that most of this plot corresponds to Ω values much less than π_m. These curves are also of the form of those determined experimentally[10,51,54] except that the experimental intercept found is usually positive.

The methods of plotting experimental results described in this last Section have been quite widely used in liquid electrochemical situations but not appreciably for analysis of frequency-response data on solids. When such data indicate a C_P slope of $m\sim 0.5$, it should be profitable to test the data against the equations of this Section and, when agreement is found, determine the values of the various parameters entering the equations. In general, comparison of experimental results with the theoretical results of the present paper should, in pertinent cases, permit the determination of values of the following physically significant parameters: μ_n, μ_p; z_n, z_p; r_n, r_p; ξ_n, ξ_p; n_i, p_i; C_g, R_∞; M and ε. Measurements at several temperatures should then allow estimates of the thermal activation energies associated with such quantities as ξ_n and ξ_p to be obtained.

LIST OF SYMBOLS

A. Major subscripts

- i Designates an intrinsic or series "interface" quantity; also used as index with i = n or p
- n Designates quantity associated with negative mobile charged species
- p Designates quantity associated with positive mobile charged species
- N Normalization of impedances and resistances with R_∞, of admittances and conductances with $G_\infty \equiv R_\infty^{-1}$, and of capacitances with C_g
- P A parallel quantity
- S A series quantity; also indicates a plateau region quantity
- T Stands for "total"
- 0 Designates either a static quantity or the zero-frequency limit of a frequency-dependent quantity
- ∞ The value of a quantity in the limit of high frequencies (*i.e.*, $\Omega \gg 1$)

B. Major symbols in text

Numbers in parentheses indicate equations where the symbol is used or defined.

- A $(4G_{WPN}C_{WSN})^{-\frac{1}{2}}$; normalized Warburg parameter; (6), (31)
- A_0 Warburg parameter; (5), (42), (50), (97)
- C_{CP} Frequency-independent part of $C_{\theta P}$
- C_{CS} Frequency-independent part of $C_{\theta S}$
- C_d Apparent double-layer capacitance in the supported case; see Fig. 20
- C_g Geometric capacitance/unit area; $\varepsilon/4\pi l$
- C_i "Interface" capacitance/unit area; the series capacitance associated with Z_i; (60)
- C_{iS} "Interface" capacitance/unit area in the plateau region
- C_K $(C_{WP}+C_{\theta P})$
- C_P Total parallel capacitance/unit area; associated with Y_T; (102). Note: $C_{P0} \equiv C_0 \equiv C_{i0}+C_g$
- C_{PS} Total parallel plateau capacitance/unit area
- C_{WP} $(2A\Omega^{\frac{1}{2}})^{-1}C_g$
- C_{WS} $(A\Omega^{\frac{1}{2}})^{-1}C_g$
- $C_{\theta P}$ See eqns. (58), (63), and (67)
- $C_{\theta S}$ See eqns. (65) and (72)
- D_i Diffusion coefficient; for positive carriers i = p; for negative i = n
- G_{CP} Frequency-independent part of $G_{\theta P}$
- G_D Frequency-independent parallel discharge conductance/unit area; see Fig. 1; $G_{DN} \equiv \varepsilon_n[1+(2/r_n)]^{-1}+\varepsilon_p[1+(2/r_p)]^{-1}$
- G_E $(g_s G_\infty/g_p g_n) \equiv (G_\infty - G_D) \equiv R_E^{-1}$; $G_{EN} \equiv \varepsilon_n[1+(r_n/2)]^{-1}+\varepsilon_p[1+(r_p/2)]^{-1}$; see Fig. 1
- G_K $(G_{WP}+G_{\theta P})$
- G_P Total parallel conductance/unit area; associated with Y_T; (102). Note: $G_{P0} \equiv G_D$; $G_{P\infty} \equiv G_\infty$
- G_{pn} $[(g_p-g_n)/g_p g_n]^2$
- G_{WP} $\Omega^{\frac{1}{2}}G_\infty/2A$
- $G_{\theta P}$ See eqns. (58), (62) and (66)

G_∞ Bulk conductance/unit area; R_∞^{-1}
H_{pn} $[(g_z^2 - g_s)/(g_p - g_n)^2]$
L_D Debye length in the present intrinsic case
M $(l/2L_D)$
N $(5MA^2)^{-1}$
R_{CS} Frequency-independent part of $R_{\theta S}$
R_D G_D^{-1}
R_E Frequency-independent series resistance-unit area; G_E^{-1}
R_i "Interface" series resistance-unit area; associated with Z_i; (60)
R_S $(R_E + R_i)$
R_{WS} $AR_\infty/\Omega^{\frac{1}{2}}$
R_θ Equilibrium charge transfer resistance-unit area in supported case; see Fig. 20
$R_{\theta S}$ See eqns. (64) and (71)
R_∞ G_∞^{-1}
T Absolute temperature
X $2^{\frac{1}{2}}(AM\Omega^{\frac{1}{2}})^{-1}$; (98)
Y_i Z_i^{-1}
Y_T Total admittance/unit area of the system; (102)
Y_W Z_W^{-1}
Y_θ $(G_{\theta P} + i\omega C_{\theta P})$; (59)
Z_i "Interface" impedance-unit area; (14), (60)
Z_j Components of Z_T; $j = 1,2,3$; (4′)
Z_T Y_T^{-1}; (3)
Z_W $A_0(1-i)/\omega^{\frac{1}{2}}$; Warburg impedance
Z_θ $[R_{\theta S} + (i\omega C_{\theta S})^{-1}]$; (61)
a $(\delta_p^2/\varepsilon_p) + (\delta_n^2/\varepsilon_n)$
b $\delta_n\delta_p/\varepsilon_n\varepsilon_p$
c $(\delta_n/\varepsilon_n) - (\delta_p/\varepsilon_p)$
e Protonic charge
g_i $1 + (r_i/2)$; i = e ($r_n = r_p$), n, or p
g_s $g_n\varepsilon_p + g_p\varepsilon_n$
g_z $g_n\delta_p + g_p\delta_n$
k Boltzmann's constant
k_i Apparent standard heterogeneous rate constants for the supported case; i = n or p
l Distance of separation of plane-parallel electrodes
m Exponent in ω^{-m} response
n Concentration of negative mobile charges
p Concentration of positive mobile charges
r $M[\coth(M)]$
r_e Designation of common value of r_p and r_n when they are equal
r_n Dimensionless discharge parameter for negative charges
r_p Dimensionless discharge parameter for positive charges
z_n Valence number for negative mobile charges
z_p Valence number for positive mobile charges
Ω Normalized radial frequency; $\omega\tau_D$
δ_n $(1 + \pi_z^{-1})^{-1} \equiv z_n/(z_n + z_p)$

δ_p $(1+\pi_z)^{-1} \equiv z_p/(z_n+z_p)$
ε Dielectric constant of the bulk material
ε_n $(1+\pi_m^{-1})^{-1} \equiv \mu_n/(\mu_n+\mu_p)$
ε_p $(1+\pi_m)^{-1} \equiv \mu_p/(\mu_n+\mu_p)$
Λ $M\Omega^{\frac{1}{2}}$
μ_i Mobility; i=n or p
ξ τ_r/τ_D
ξ_i $(D_i/l)r_i$; i=n or p; effective rate constants
ξ_{ne} Effective rate constant in unsupported case; (110)
π_m Mobility ratio; μ_n/μ_p
π_z Valence number ratio; z_n/z_p
τ_D Dielectric relaxation time; $C_g R_\infty$
τ_E $R_E C_i$
τ_r Recombination time constant
τ_S $(R_E+R_i)C_i$
ω Radial frequency of the applied sinusoidal voltage

SUMMARY

The frequency response is considered of a two-electrode linearized system containing a single positively charged species and a single negatively charged species. These species may have arbitrary valences and mobilities and may individually react at the electrodes. The results follow from a detailed solution of the equations of charge motion given earlier. Normalized response is exhibited for this unsupported, intrinsic-conduction situation for a wide range of mobility ratios, valence number ratios, and reaction rate ratios. Results are given in the form of specific formulas, impedance-plane plots, and the dependences on normalized frequency of series and parallel resistive and capacitative components of the normalized total impedance of the system.

Impedance-plane plots exhibit from one to three connected arcs, depending on the specific situation. Approximate Warburg frequency response appears for the "interface" impedance over a certain frequency region when normalized reaction rate parameters differ, but it only shows up strongly in the total impedance when the mobility ratio departs appreciably from unity as well. Under such conditions, a plateau region, where the total parallel capacitance remains essentially independent of frequency over a wide frequency range, may appear at frequencies just above the Warburg region. The plateau capacitance is close to but not identical to the conventional double-layer capacitance present when both species of charge are completely blocked. In incomplete blocking cases, however, this double-layer capacitance only makes a significant appearance in the approximate equivalent circuit under slow reaction conditions; it is thus not present when one of the reaction rate constants is infinite.

In general, the system can show ω^{-m} frequency response for the parallel capacitance over a wide frequency range with $0 \leqslant m \leqslant 2$, and with the experimentally common regions where $m \cong 0$, 0.5, 1.5, and 2 especially likely. Particular attention is given to deviations from ideal Warburg behavior which lead to a combined charge-transfer and heterogeneous chemical reaction resistance. Results are

compared to those from conventional supported treatments and show both important similarities and differences. Finally, several new equivalent circuits are presented which are pertinent in various frequency ranges for the unsupported situation.

REFERENCES

1 J. R. Macdonald, *Trans. Faraday Soc.*, 66 (1970) 943.
2 J. R. Macdonald, *J. Chem. Phys.*, 54 (1971) 2026.
3 J. R. Macdonald, *J. Electroanal. Chem.*, 32 (1971) 317.
4 J. R. Macdonald, *J. Chem. Phys.*, 58 (1973) 4982; 60 (1974) 343.
5 J. R. Macdonald, *J. Phys. Chem. Solids*, to be submitted.
6 D. O. Raleigh, *Phys. Stat. Sol.*, 4 (1971) 215.
7 J. R. Macdonald, *J. Chem. Phys.*, 22 (1954) 1317.
8 T. S. Gray, *Applied Electronics*, John Wiley, New York, 1954, pp. 528, 578, 579.
9 K. S. Cole and R. H. Cole, *J. Chem. Phys.*, 9 (1941) 341.
10 R. de Levie, *Electrochim. Acta*, 10 (1965) 395.
11 J. R. Macdonald, *J. Chem. Phys.*, 23 (1955) 275.
12 J. H. Sluyters, *Rec. Trav. Chim. Pays-Bas*, 79 (1960) 1092.
13 R. P. Buck and I. Krull, *J. Electroanal. Chem.*, 18 (1968) 387.
14 M. J. D. Brand and G. A. Rechnitz, *Anal. Chem.*, 41 (1969) 1185; 41 (1969) 1788; 42 (1970) 478.
15 H. Moreira and R. de Levie, *J. Electroanal. Chem.*, 29 (1971) 353.
16 A. Caprani, I. Epelboin and Ph. Morel, *J. Electroanal. Chem.*, 43 (1973) App. 2.
17 R. Yu. Bek and G. N. Soria, *Elektrokhimiya*, 8 (1972) 1795.
18 J. L. Blue, *Bell Syst. Tech. J.*, 51 (1972) 889.
19 J. R. Macdonald, *Phys. Rev.*, 91 (1953) 412; 92 (1953) 4.
20 J. R. Macdonald, *J. Chem. Phys.*, 29 (1958) 1346; 30 (1959) 806.
21 J. R. Macdonald, *J. Appl. Phys.*, to be published.
22 J. H. Beaumont and P. W. M. Jacobs, *J. Phys. Chem. Solids*, 28 (1967) 657.
23 R. J. Friauf, *J. Chem. Phys.*, 22 (1954) 1329.
24 R. Michel, G. Asch and M. Maitrot, *C.R. Acad. Sci. (Paris)*, 270 (1970) 1644; R. Michel, M. Maitrot and R. Madru, *J. Phys. Chem. Solids*, 34 (1973) 1039.
25 G. Cochrane and N. H. Fletcher, *J. Phys. Chem. Solids*, 32 (1971) 2557.
26 R. D. Armstrong and W. P. Race, *J. Electroanal. Chem.*, 33 (1971) 285; 34 (1972) 244.
27 A. R. Allnatt and S. J. Sime, *J. Phys. C: Solid State Phys.*, 5 (1972) 134.
28 M. C. Lancaster, *J. Phys. D: Appl. Phys.*, 5 (1972) 1133.
29 S. P. Mitoff and R. J. Charles, *J. Appl. Phys.*, 43 (1972) 927.
30 J. R. Macdonald, *J. Appl. Phys.*, 44 (1973) 3455.
31 S. P. Mitoff and R. J. Charles, *J. Appl. Phys.*, 44 (1973) 3786.
32 G. M. Tibensky and H. J. Wintle, *J. Phys. Chem. Solids*, 33 (1972) 191.
33 N. Maeno, *J. Appl. Phys.*, 43 (1972) 312; *Can. J. Phys.*, 51 (1973) 1045; *Contrib. Inst. Low Temp. Sci., Hokkaido Univ., Ser. A*, 25 (1973) 1.
34 M. A. Seitz, R. T. McSweeney and W. M. Hirthe, *Rev. Sci. Instrum.*, 40 (1969) 826; see also P. A. Tick and D. Johnson, *Rev. Sci. Instrum.*, 44 (1973) 798.
35 J. R. Macdonald, *J. Electroanal. Chem.*, 47 (1973) 182.
36 K. J. Vetter, *Electrochemical Kinetics*, Academic Press, New York, 1967, pp. 200–204.
37 J. E. B. Randles, *Dicuss. Faraday Soc.*, 1 (1947) 11.
38 M. Sluyters-Rehbach and J. H. Sluyters in A. J. Bard (Ed.), *Electroanalytical Chemistry, Vol. 4*, M. Dekker, New York, 1970, p. 15.
39 Ref. 36, p. 154.
40 P. Delahay in P. Delahay (Ed.), *Advances in Electrochemistry and Electrochemical Engineering, Vol. 1*, Interscience, New York, 1961, p. 240.
41 Ref. 38, p. 20.
42 Ref. 38, p. 32.
43 Ref. 38, p. 18.
44 Ref. 36, pp. 346–347.

45 J. R. Macdonald, *J. Electroanal. Chem.*, 40 (1972) 440.
46 D. C. Grahame, *J. Electrochem. Soc.*, 99 (1952) 370C.
47 Ref. 40, pp. 267, 269.
48 P. J. Hillson, *Trans. Faraday Soc.*, 50 (1954) 385.
49 D. L. Hill, G. J. Hills, L. Young and J. O'M. Bockris, *J. Electroanal. Chem.*, 1 (1959/60) 79.
50 R. D. Armstrong, D. F. Porter and H. R. Thirsk, *J. Electroanal. Chem.*, 14 (1967) 17.
51 R. D. Armstrong, W. P. Race and H. R. Thirsk, *J. Electroanal. Chem.*, 14 (1967) 143.
52 L. D. Yushina, S. V. Karpachev and Yu. S. Fedyaev, *Elektrokhimiya*, 8 (1972) 788.
53 D. L. Hill, K. W. Fung, S. Hsieh and H. L. Lee, *J. Electroanal. Chem.*, 38 (1972) 57.
54 L. S. Leonova, E. A. Ukshe and V. V. Evtushenko, *Elektrokhimiya*, 8 (1972) 1596.
55 Ref. 36, pp. 350–352.
56 Ref. 36, p. 261.